La Secuencia Principal de los cuásares y la emisión en Rayos-X

(The quasar Main Sequence and the X-ray emission)

Trabajo de Fin de Máster
para acceder al

MÁSTER INTERUNIVERSITARIO EN FÍSICA DE PARTÍCULAS Y DEL COSMOS

Autor: Silvia García Soto

Director\es: Amalia Corral Ramos
Ascensión del Olmo Orozco

Septiembre - 2023

Resumen

Los Núcleos Galácticos Activos (AGN) son objetos diversos con una amplia fenomenología. La diversidad espectroscópica de los AGN de tipo 1 y de los cuásares en particular, ha llevado al desarrollo del el formalismo 4DE1 y la Secuencia Principal de los cuásares, basada en 4 parámetros de los cuales el relacionado con la emisión de Rayos-X, el índice espectral blando (Γ_{soft}), es el menos estudiado. En las últimas décadas, la disponibilidad de datos espectroscópicos de estos objetos ha aumentado gracias a cartografiados como el Sloan Digital Sky Survey (SDSS) y a las observaciones realizadas por XMM-Newton, que abren la posibilidad de un análisis de los AGN en diferentes longitudes de onda.

El objetivo de este trabajo es estudiar las propiedades espectrales en Rayos-X de una muestra de cuásares según su clasificación espectral en la secuencia principal, diferenciando entre la población A (altos acretores) y B (menor tasa de acreción). El estudio del exceso de Rayos-X blandos en la banda 0.3-2 keV (soft excess) observados en cuásares con alta acreción y normalmente modelado con un cuerpo negro es especialmente interesante. Para ello, hemos encontrado las contrapartidas en rayos-X de una muestra óptica de cuásares en el catálogo 4XMM-DR12, obteniendo una muestra final con 207 fuentes con datos espectrales.

Hemos realizado un análisis de los espectros de rayos-X usando estadística Bayesiana y considerando cuatro modelos: una ley de potencias en los rayos-X duros; después incluyendo todo el rango 0.3-10 keV, una ley de potencias absorbida; una ley de potencias absorbida con una componente de cuerpo negro para cuantificar el soft excess; y una doble ley de potencias. Los ajustes se realizan con la herramienta BXA (Análisis de rayos X bayesiano) lo que nos ha permitido estudiar las distribuciones posteriores de los parámetros para cada población.

Este trabajo presenta por primera vez un estudio detallado de las propiedades espectroscópicas en rayos-X de los AGN tipo 1 en la secuencia principal de los cuásares. Se ha llevado a cabo un total de 602 ajustes espectrales de 207 objetos, y hemos encontrado un modelo aceptable para 177 objetos de la muestra, que es representativa de los tipos espectrales definidos en la secuencia principal de los cuásares; mientras que para las 30 fuentes restante un análisis individual es necesario.

Hemos encontrado los siguientes resultados: a) la ley de potencias en la banda de rayos X duros es una primera evidencia de una diferencia significativa en el índice espectral de las dos poblaciones y esta distinción es aún más significativa cuando consideramos la ley de potencias absorbida en el rango de energías 0.3-10 keV; b) la diferencia entre las poblaciones A y B incrementa al añadir la componente de cuerpo negro para modelar el soft excess (0.5-2 keV), dando valores $\Gamma \sim 2.11$ (pob. A) y $\Gamma \sim 1.86$ (B); c) la diferencia se observa también en los subtipos espectrales, con valores similares de Γ para los tipos A1 y B1, incrementando para los tipos A2 y xA (altos acretores) y disminuyendo para los B+ y B++ (agujero negro más masivo y menor tasa de acreción); d) una relación entre Γ [0.3-10 keV] y RFeII (razón entre la intensidad de la línea FeIIλ4570Å y Hβ , RFeII = I(FeIIλ4570Å)/I(Hβ)), relacionado con la tasa de acreción del agujero negro; e) la

importancia del cuerpo negro es mayor para la población A, como demuestra la razón entre luminosidades L_{bb}/L_{pl}. La mayoría de objetos con $L_{bb}/L_{pl} > 1$ son extremos acretores.

Palabras clave: Núcleos Activos de Galaxias, Secuencia Principal de los Cuásares, XMM-Newton, Exceso en Rayos-X blandos, Formalismo 4DE1

Abstract

Active Galactic Nuclei (AGN) are diverse objects with rich phenomenology. The spectroscopic diversity of type 1 AGN and quasars in particular, has led to the development of the 4DE1 formalism and the quasar main sequence, based on 4 parameters from which the one related to the X-ray emission, the soft photon index (Γ_{soft}), is the least studied. Over the last decades, the availability of spectroscopic data of these objects has increased thanks to surveys like the Sloan Digital Sky Survey (SDSS) and the observations made by XMM-Newton, which open the possibility of a multi-wavelength analysis of AGN.

The aim of this work is to study the X-ray spectral properties of a sample of quasars in relation to their spectral classification in the main sequence, differentiating between Population A (high accretors) and B (with lower accretion rates). Of particular interest is the study of the X-ray soft excess in the 0.3-2 keV band observed mainly in high accreating quasars and usually reproduced using a black-body spectrum.

In order to accomplish this, we have found the X-ray counterparts of an optically selected sample of quasars in the 4XMM-DR12 catalogue, obtaining a final sample of 207 sources with spectral data. We have carried out an X-ray spectral analysis by using Bayesian statistics and considering four models: a power-law in the hard X-rays; then considering the whole range 0.3-10 keV, an absorbed power-law; an absorbed power-law with a black-body component to quantify the possible soft excess; and a double power-law. The fits are performed using the tool BXA (Bayesian X-ray Analysis) which has permitted us to study the posterior distributions of the parameters for each population.

This work presents for the first time a detailed study of the X-ray spectroscopic properties of type 1 AGN along the main sequence of quasars. A total of 602 spectral fittings of 207 objects have been carried out, and we have found a satisfactory model for 177 objects of the sample that its representative of all the spectral types defined in the main sequence of quasars while the remaining 30 sources need a more individual analysis.

We have found the following results: a) the power-law in the hard band gives a first indication of a significant difference in the photon index of both populations and this distinction becomes more significant when considering the absorbed power-law in the 0.3-10 keV energy range; b) the difference between populations A and B increases when adding the black-body component to model the soft excess ($\sim$0.5-2 keV), resulting in $\Gamma \sim 2.11$ (pop. A) and $\Gamma \sim 1.86$ (B); c) the difference is present as well in the spectral sub-types, with similar values for types A1 and B1, increasing noticeably for types A2 and xA (high accretors) and diminishing for types B+ and B++ (quasars with higher M_{BH} and lower

accretion rates); d) a relation between the Γ [0.3-10 keV] and R_{FeII} (intensity ratio of the optical FeIIλ4570Å feature and Hβ, $R_{FeII} = I(FeII\lambda 4570Å)/I(H\beta)$), closely related to the accretion rate of the black hole; e) the significance of the black-body is higher for Population A, as shown by the luminosity ratio L_{bb}/L_{pl}. Almost all objects with $L_{bb}/L_{pl} > 1$ are extreme accretors.

Key words: Active Galactic Nuclei, Quasar Main Sequence, XMM-Newton, X-ray Soft Excess, 4DE1 Formalism

Contents

1 Introduction

1.1 Motivation

Active Galactic Nuclei (AGN) are some of the brightest objects in the universe. The study of these energy sources at the center of galaxies is determinant to understand their evolution as well as all the physical phenomena that take place around the AGN. In the last decades the increasing number of observations at different wavelengths have shown that AGN are diverse objects with rich phenomenology, which has resulted in a wide range of classes that try to explain their properties.

The study of type 1 AGN and quasars (QSO) in particular at X-ray energies is also of great importance in order to assess the relation between the X-ray intrinsic spectral emission and the accretion properties of the AGN, namely the Eddington ratio, λ_{Edd}.

The widely accepted model for AGN consists in the presence of an accreting, supermassive ($\geq 10^6 M_\odot$) black hole (SMBH) in the center of the galaxy that accounts for the high luminosities observed, up to $L_{bol} \approx 10^{48}\, erg\, s^{-1}$, with an accretion disk surrounded by the corona (electron plasma) and a torus made of gas and dust. Some AGN can also show collimated outflows radiating from the center producing radio emission (jets). These different components provide for emission in the whole electromagnetic spectrum, with different bands being sensitive to the different structures and processes taking place in AGN.

The material from the host galaxy that is falling into the black hole heats the accretion disk around it ($T \sim 10^6 - 10^7\, K$), resulting in thermal radiation emitting from near-IR (outer regions of the disk) to soft X-rays (inner regions at higher temperatures). The UV/optical continuum shows a power-law profile with a characteristic "Big Blue Bump" thought to be caused by the disk (peaking at $\lambda = 1000 - 4000$ Å) and a break at around 1000Å.

The emission from the accretion disk is also responsible for some secondary processes that emit radiation at different energies. In the UV/optical range, AGN display emission lines coming from two different regions and that are observable depending on the inclination of the torus with respect to our line of sight, according to the Unified Model for AGN, as shown schematically in Figure 1.

Broad emission lines originate in the Broad Line Region (BLR), between the torus and the SMBH (and therefore visible if the center of the AGN is in our line of sight and not absorbed/obscured by the material within the torus), and they have widths of a few $1000\, km\, s^{-1}$. Narrow lines with widths between $300 - 1000\, km\, s^{-1}$, on the other hand, come from a larger region ($R \sim 10^2\, pc$) extending above and below the plane of dust around the SMBH called the Narrow Line Region (NLR) (Urry and Padovani, 1995; Padovani et al., 2017).

In this way, broadly speaking, the variety of AGN can therefore be explained by the effect of orientation with respect to the torus. In type 1 AGN, the view towards the active nucleus and the BLR is unobstructed, while for type 2 the dust obscures the UV/optical emission

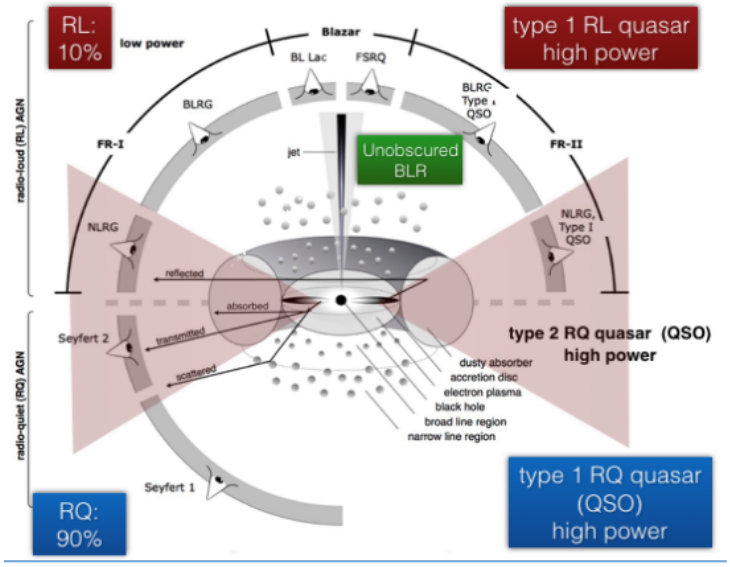

Figure 1: Schematic representation showing the AGN unification model annotated by P. Marziani and A. del Olmo. Original image from Beckman and Shrader (2012), graphic by Marie-Luise Menzel.

of the accretion disk and only narrow lines from the NLR are observed. Also classically, type 1 AGN at high luminosity are named quasars, while at low luminosity (for absolute magnitudes[1] M_B fainter than ~ -23) the host galaxy is well visible and the objects have historically been called Seyfert 1.

There is also X-ray emission different from the thermal emission of the innermost region of the accretion disk that is caused by its interaction with the corona, a plasma of hot ($kT \sim 100\,keV$) electrons located above the SMBH. In this compact and optically thin corona, the soft photons (optical, UV and X-ray) from the accretion disk gain energy through inverse Compton scattering in a process known as "Comptonization". The comptonized photons give raise to a X-ray non-thermal emission with a power-law profile of the form:

$$f_\nu \propto \nu^{-\Gamma} \tag{1}$$

Where f_ν is the specific flux (incident energy per unit of area and time) emitted at a frequency ν. Commonly used units for flux in astronomy are erg $\mathrm{cm}^{-2}\,\mathrm{s}^{-1}\,\mathrm{Hz}^{-1}$ or the *Jansky*[2], while the preferred units in X-ray astronomy are photons $\mathrm{cm}^{-2}\,\mathrm{s}^{-1}\,\mathrm{keV}$.

The exponent Γ is the slope of the power-law, known as "photon index" and with typical values of $\Gamma \sim 1.8 - 2$. This direct X-ray emission constitutes a continuum in the SED that extends from 1 keV to ∼100 keV.

[1] Magnitudes are quantities used in astronomy that measure the brightness of an object in a wavelength range. The scale is logarithmic and has two definitions: either as dependent on the distance and extinction (apparent magnitude m) or as the intrinsic brightness (absolute magnitude M).

[2] $1\,\mathrm{Jy} = 10^{-23}\,\mathrm{erg\ cm}^{-2}\,\mathrm{s}^{-1}\,\mathrm{Hz}^{-1}$

There is also a contribution of reprocessed comptonized photons when they are absorbed by cold ($T < 10^6\,K$), optically thick (column densities of around $N_H = 10^{24}\,cm^{-2}$) material like the accretion disk, the torus or the BLR. This leads to a reflection hump with a maximum at $\sim 20 - 30\,\mathrm{keV}$ and a cut-off at $\sim 4 - 5$ keV produced by the photoelectric absorption of the lower energy incident radiation. Photoelectric absorption due to neutral or not fully ionized gas is energy dependent, starts being effective at $N_H \sim 10^{21}\,cm^{-2}$ and is not significant at energies above 10 keV (for Compton−thin column densities, $N_H < 10^{24}\,cm^{-2}$). Emission lines are also an important feature, from which Fe Kα at 6.4 keV is the strongest one.

In addition to these components there is a "soft excess" observed in a large fraction of AGN that consists in an excess of X-ray emission at energies < 2 keV with respect to the extrapolation to low energy of the hard power-law continuum. This X-ray soft excess is usually fitted using a black-body spectrum (only as a phenomenological model) which gives a characteristic temperature $kT \sim 0.1 - 0.2\,\mathrm{keV}$ that seems to be constant over a wide range of AGN with different luminosities and black hole masses. It was first discovered by the EXOSAT satellite in the 1980s and has since remained a topic of discussion, with two main models trying to explain the origin of this emission (Petrucci et al., 2018; Yu et al., 2023).

One of them is the warm Comptonization model and it assumes a second cooler ($kT \sim 0.5 - 1\,\mathrm{keV}$) and optically thick ($\tau \sim 5 - 10$) corona, that would be responsible for the Comptonization of UV photons from the disk resulting in the soft excess. The second model is the relativistic blurred disc-reflection model. This one explains the soft excess as emission lines from the reflection component that are blurred due to relativistic effects near the SMBH and is supported by the evidence of soft X-ray reverberation lags.

The different components of the X-ray spectrum mentioned above are shown in Figure 2.

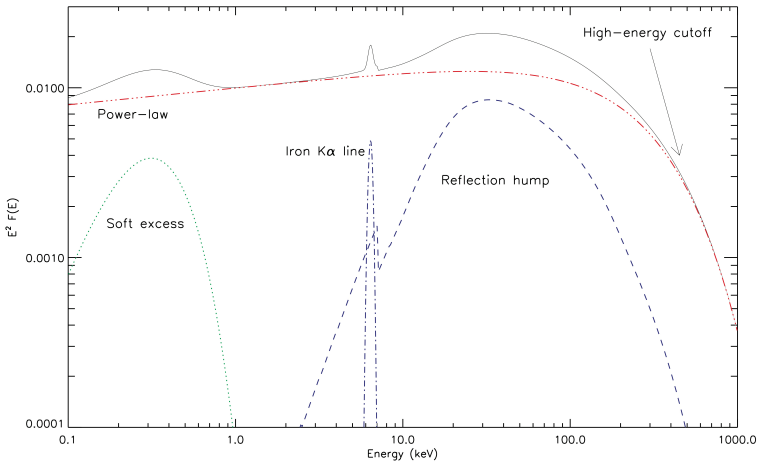

Figure 2: Typical 0.1-1000 keV spectrum of an unabsorbed AGN. Image reference: Ricci et al. 2011, PhD thesis (https://www.isdc.unige.ch/~ricci/Website/AGN_in_the_X-ray_band.html)

Types 1 and 2 AGN can also be distinguished using X-ray observations. In this case, the

distinction is made based on the intrinsic absorption measured as the column density of hydrogen (N_H) in the line of sight. In general, at low redshift, type 1 AGN show values of column density $N_H < 10^{22}\, cm^{-2}$ meanwhile objects with higher values of absorption are usually classified optically as type 2 AGN (Seyfert 1.9 or 2).

More than fifty years after the discovery of AGN, and quasars in particular, a general accepted idea about their nature exits and the standard paradigm sees quasars as driven by gravitational accretion onto a central supermassive black hole (SMBH) surrounded by an accretion disk which feeds the SMBH with gaseous material, although a fundamental empirical understanding is still lacking (see e.g. Marziani et al., 2018a, and references therein).

In the last thirty years there has been a huge increase in the availability of obtaining spectroscopic data for AGN specially thanks to the advent of new surveys as the Sloan Digital Sky Survey (SDSS) (see e.g. Lyke et al., 2020, for DR16). However, most of the spectra contained in these surveys have in general a low signal-to-noise ratio[3] (S/N < 10), that has led to the impression that all quasars are similar despite the diversity observed in their spectroscopic properties. Optical surveys have been paired with matching X-ray and radio surveys, providing multi-wavelength data for a fraction of optically selected sources.

How are these new data organized? Do all quasars respond to the same pattern and therefore can they be mixed with each other under the assumption that all quasars are the same? Even if the fundamental physical process is the same, the phenomenology is not, and hints at differences related to accretion mode and balance between gravitation and radiation. In fact, the nature of the many differences seen in quasar spectra is at present a key topic of interest (Marziani et al., 2018a; Wolf et al., 2020; Temple et al., 2023).

In the last decades, a new framework for the spectroscopic diversity observed in type 1 AGN has been developed and proven to be of interest for the study of quasars and its properties. This is the 4DE1 formalism and the quasar main sequence that will be introduced in the next section.

1.2 4DE1 Parameter Space and The Quasar Main Sequence

First quasar observations started in the 1960s (see e.g. Greenstein and Schmidt, 1964), although evidences of an additional strong emission in the center of a few galaxies was previously found in the 1940s (Seyfert, 1943). In the optical and UV ranges, quasars are characterised by a bright point-like core and bluer appearance, and among their most noticeable spectral features are the presence of broad emission lines (with widths 1000–20000 km s^{-1}) and the "Big Blue Bump" corresponding to an excess flux relative to the underlying power-law continuum (very distinct from the stellar continuum of normal galaxies) and interpreted as the first observational evidence of the thermal emission from the accretion disc.

[3]Signal-to-noise ratio (S/N) is a quantity that compares the level of the signal of an object to the level of background noise.

Quasars are observed over the entire range of the electromagnetic spectrum from radio up to gamma-rays (see e.g., Padovani et al., 2017). Also two different classes have been historically defined on the basis of its radio emission, which is a signature of relativistic outflows that produce synchrotron radiation. Depending on the ratio of the radio to optical emissions (the radio-loudness parameter) and presence or absence of strong and extended relativistic radio jets the two classes are called respectively radio-loud (RL) and radio-quiet (RQ). Around 10% of quasars are classified as radio-loud (Kellermann et al., 2016).

As mentioned, type 1 AGN spectra show broad emission lines with a wide variety of strengths, line profiles, ionization levels and velocity widths. Pioneering works about the systematic trends of quasar spectra (Boroson and Green, 1992; Marziani et al., 1996) showed that they do not scatter randomly around an average spectrum and led to the development of a 4-Dimensional Eigenvector-1 empirical formalism (4DE1) that emerged as a powerful tool to organize the observed spectroscopic diversity (Sulentic et al., 2000b; Marziani et al., 2018b, for a recent review).

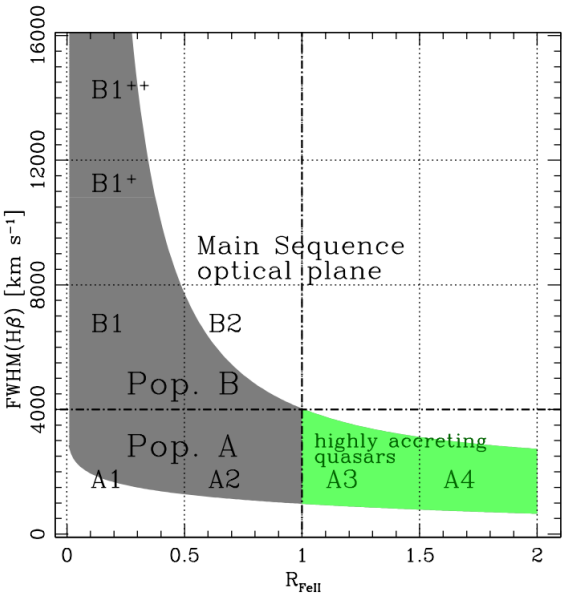

Figure 3: A sketch representing the optical plane (FWHM(Hβ) vs. R_{FeII}) of the 4DE1 scheme, the so-called quasar main sequence (MS), where the subdivisions correspond to the different spectral types along the sequence (see e.g., Sulentic et al., 2000a; Marziani et al., 2001; Marziani, P. et al., 2019; Ganci et al., 2019) for the two populations of quasars (A and B). Green area marks the highly accreting, extreme Population A, quasars

Eigenvector 1 (E1) was originally defined from a Principal Component Analysis (PCA) of 87 low-redshift QSOs, involving an anti-correlation between optical FeII intensity, FWHM of Hβ and peak intensity of [OIII]5007Å (Boroson and Green, 1992). The 4DE1 scheme expanded the original E1 parameters and makes use of 4 independent observational properties, in optical, UV and X-rays: 1) the Full Width Half Maximum (FWHM) of broad Hβ profile; 2) the ratio of the intensities of the optical FeIIλ4570Å and broad Hβ, RFeII = I(Feii4570Å)/I(H); 3) the soft X-ray photon index, and 4) the velocity shift the CIVλ1549Å

emission line, that measures the prominence of an outflowing/wind component. The two first parameters define the optical plane of the 4DE1, known as **the quasar Main Sequence** (Marziani et al., 2001; Shen and Ho, 2014; Wolf et al., 2020). Figure 3 provides a diagram of the main sequence optical plane.

Exploration of the 4DE1 parameter space and its optical main sequence gave rise to the concept of two quasar populations, A and B, and a sequence of spectral types dividing the optical main sequence into a grid of bins of FWHM(Hβ) and FeII emission strength. Population A quasars generally have FWHM(Hβ) $\leq$ 4000 km s^1, Lorentzian profiles in the emission lines, tend to have RFeII larger than 0.5 and important blue shifts in CIV. It includes Narrow Line Seyfert 1 and is mostly populated by radio-quiet quasars. On the other hand, Population B quasars show a very wide range of FWHM(Hβ), with values higher than 4000 km s^1, Gaussian line profiles (with two components: a broad and an additional very broad redshifted component), RFeII < 0.5 and not showing significant blue shifts in CIV. In general the radio-loud sources are located in the Population B domain of the MS, while the radio-quiet are found in both populations. Recent studies tried to evaluate a relation between Γ_{soft}, the width of the Hβ line and the Fe II prominence, finding that higher values of the X-ray soft excess are concentrated in highly accreting Population A quasars (Panda and Marziani, 2023).

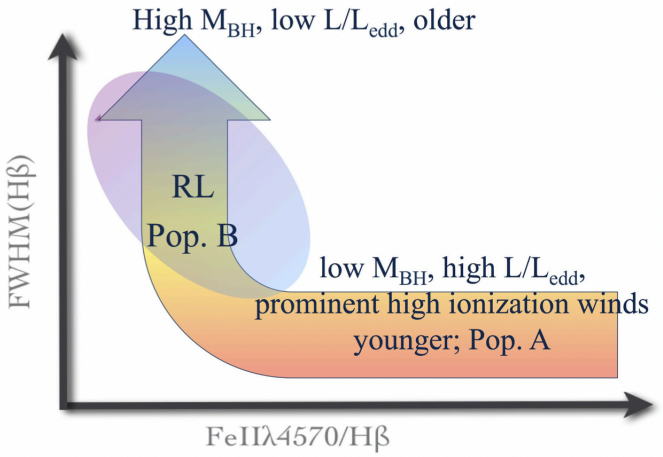

Figure 4: Possible evolutionary interpretation of the 4DE1 optical plane. Arrow indicates the direction of increasing evolutionary state. Low accreting Population B sources are interpreted as the oldest quasars with lowest accretion rates and largest M_{BH}. Adapted from Sulentic et al. (2008)

Apart from these parameters that define populations A and B, the relevance of the main sequence also resides in that several observational and physical properties, such as those related to the accretion rate, black hole mass, the prominence of outflows or the prevalence of jetted sources, change systematically along it. A possible evolution scenario from Population A to B is shown in Figure 4, going from the "wind-dominated" extreme Pop. A quasars, with intense FeII emission and highly accretion rates to the more massive BH, low accreting "disc-dominated" Population B quasars.

1.3 Objectives

The quasar main sequence is based on 4 parameters (FWHM(Hβ), R_{FeII}, CIV(1549Å) and the soft X-rays Γ; as mentioned in the previous section) from which the one related to the X-ray emission is the least studied. Recent spectral data catalogs from X-ray observatories such as XMM-Newton, Chandra, Swift, etc. and surveys like the Sloan Digital Sky Survey (SDSS) offer access to the spectra of thousands of sources, including quasars, opening the possibility to carry out an analysis centered on the X-ray properties of these objects and their importance in the differentiation of the populations. A particularly interesting feature is the soft X-rays excess that was first discussed by Singh et al. (1985) that can be interpreted as extreme changes in the thermal emission from the accretion disk that change the reprocessed emission observed in X-rays, and therefore is expected to dominate on sources that are accreting material at a higher rate.

After the introduction of $\Gamma_{\rm soft}$ by Sulentic et al. (2000a) as a possible key parameter in the explanation of the spectral diversity observed in type 1 AGN, not much new X-ray data became available until the advent of XMM-Newton. Some empirical evidence based mainly on ROSAT data for a few sources (Sulentic et al., 2008) showed that quasars with soft X-ray excess were mainly high accreting quasars. Now thanks to the extensive observations with XMM-Newton, which provides spectra covering the 0.3 - 10 keV range, we have the possibility to analyse in detail the X-ray spectral properties of optically selected samples of different populations of quasars in the 4DE1 formalism.

Therefore one of the main objectives of the present work is to quantify the X-ray properties and spectral differences of quasars, in particular the presence of a soft excess, to address fundamental questions about phenomenology and quasar physics by analysing a wide sample of quasars with different classification along the main sequence. The main objective of this work is to study the presence of this soft excess and the importance of the X-ray emission in a wide sample of quasars with different classification along the main sequence. For that, the analysis of the data will focus on:

- A general study of the properties of the X-ray emission (such as the luminosity and spectral index) in a sample of AGN by fitting different models to their spectra, making a comparison between the two populations (A and B) and their sub-types (Figure 3).
- Evaluating the existence of the X-ray soft excess in the $\sim$0.3-2 keV band that could arise from changes in the emission reprocessed by the accretion disk, especially in quasars of Population A, with a higher accretion rate. This emission arises as UV seed photons from the disk are up-scattered by a Comptonizing optically thick corona cooler than the hot corona responsible for the primary X-ray emission (Tripathi and Dewangan, 2022; Boissay et al., 2016).
- Analysing the relation between the X-ray emission and others parameters used to define the quasar main sequence, like the width of the broad component of the $H\beta$ line (FWHM($H\beta$)) and the ratio of the FeII 4570Å and $H\beta$ line fluxes (R_{FeII}).

2 Methodology

2.1 Sample Selection

For the purpose of this work, the selected sample of objects should include QSO of both Population A and B with available spectral data at X-ray energies in order to characterize their X-ray spectra and to study the excess observed around the 0.3-2 keV soft band by comparing the emission to that one of the hard X-ray band (2-10 keV) as well as its relation to the other parameters that characterize the AGN in the 4DE1 plane and their spectral type in the main sequence.

One of two data sets used to find counterparts in X-ray catalogues is a sample of sources obtained in the cross correlation of observations of the Radio Sky at Twenty-Centimeters survey (FIRST) and the Sloan Digital Sky Survey Quasar Catalog described in Ganci et al. (2019) (from here on referred to as "GAN"). The sample was analyzed discarding type 2 AGN and host galaxy contaminated spectra in order to obtain a reliable classification of the objects, resulting in 355 quasars with redshift < 1, i-band apparent magnitude $m_i < 19.5$ and bolometric luminosities between $10^{44} - 10^{47}$ erg s^{-1}, with their corresponding spectral type, radio-morphology class and radio-loudness.

The second data sample used in this work is the combination of three different studies presented in Marziani et al. (2003), Sulentic et al. (2007) and Zamfir et al. (2010), regarding type 1 AGN, where broad lines were observed. In Marziani et al. (2003) the authors present an optical analysis of 215 objects consisting in luminous Seyfert 1 and low redshift quasars, up to $z \approx 0.8$. The spectral data was obtained with different telescopes and spectrographs (ESO 1.5 m, San Pedro Martir 2.2 m, Calar Alto 2.2 m, KPNO 2.2 m and Asiago 1.82 m) while maintaining a very similar instrumental setup, providing a resolution of 4-7.5Å and a median value for the S/N of ≈ 25. They measure the rest frame equivalent width and FWHM for the Fe II$_{opt}$ blend at λ4570, Hβ, He II λ4686, and the [O III]4959, 5007ÅÅ emission lines, among other parameters from the Hβ spectral region. Sulentic et al. (2007) carried out measurements of the C IV λ1549 line broad component for 130 studied sources from the HST archival spectra with the aim to find a distinction between AGN populations A and B based on this parameter. The sources were chosen so they had reliable measures of the emission profiles and broad lines corresponding to type 1 AGN. Another part of the sample comes from Zamfir et al. (2010), where an analysis of the $H\beta$ emission line is made for ~ 470 low-redshift ($z < 0.7$) quasars from the fifth Sloan Digital Sky Survey (SDSS) Data Release. The work focuses in the optical parameters FWHM($H\beta$) and $R_{FeII} \equiv W(FeII\,4434-4684)/W(H)$ (relative strength of optical Fe II line) of sources in the luminosity regime $log\,[L_{bol}(erg\,s^{-1})] = 43-47$ and with redshifts low enough to have a good coverage of the $H\beta$ spectral region.

The resulting sample, hereinafter referred to as "ZMS", has a total of 682 sources with redshifts in the range $z \sim 0.03 - 0.9$ as well as measurements of optical parameters like FWHM($H\beta$) and R_{FeII}.

2.2 Instrumentation

2.2.1 X-ray Multi-Mirror Mission - Newton

The X-ray Multi-Mirror Mission (XMM-Newton) space observatory was launched on December 10th 1999 as part of the ESA's Horizon 2000 program and it constitutes the X-ray satellite with the largest effective area thanks to the three X-ray telescopes aboard. Two of the cameras are MOS (Metal Oxide Semi-conductor) CCD arrays while the third uses pn CCDs (PN camera), the three of them comprising the European Photon Imaging Camera (EPIC). The MOS cameras are situated behind the telescopes equipped with Reflection Grating Spectrometers (RGS) making the observations of the PN camera (corresponding to the telescope with an unobstructed beam) deeper for the same exposure time. The EPIC cameras provide a field of view (FOV) of 30' in an energy range from 0.2 to 12 keV (see XMM-Newton, for a detailed description). The EPIC cameras work on photon-counting mode, which allows the extraction of images, spectra, and light curves for almost all detected sources within a single observation. A pointing of the observatory with a mean duration of 37 ks results in the detection of up to 75 serendipitous X-ray sources, the data is then processed by the XMM-Newton Science Analysis System (SAS) developed by the XMM-Newton Survey Science Center (SSC) and put together in catalogues (Webb et al., 2020).

2.2.2 X-ray spectra

For this work, a crossmatch between the two samples of quasars from which the classification following the 4DE1 formalism was already known and the 4XMM-DR12 catalogue has been made. In order to choose the sample, from the total number of detections of the 4XMM catalogue only those with spectral data have been taken into account. The catalogue has a total of 336 columns, some of which can be used to discard observations with lower quality. In this case, the following filters have been used: i) SUM_FLAG$\leq$1 ensures that there are no spurious detections; ii) OBS_CLASS$\leq$3 is the quality classification of the observations with an area flagged as bad with respect to the total detection area smaller than 10%; iii) EP_8_DET_ML$\geq$10 refers to the maximum likelihood of the detection in the 0.2-12 keV band, and iv) EP_EXTENT_ML$\leq$1 keeps only point sources, based on the likelihood of a detection being extent, where anything below 6" is considered to be a point source.

To obtain the spectral data from the XMM-Newton Science Archive the different identifiers of the 4XMM-DR12 catalogue are used. Each entry of the catalogue corresponds to a detection identified with a unique number "DETID" while all entries for the same source have assigned a number to identify the source, "SRCID". Each observation (labelled with "OBS_ID") comprises different detections of several sources listed with a number "SC_NUM". The data for a specific observation of a source can be accessed using the OBS_ID and the SC_NUM is in hexadecimal form. This will result in several files with spectral data of the detection corresponding to different expositions using the MOS and PN cameras. Along with the spectra, the response files for the three cameras must be downloaded as well.

The next step is to prepare the spectra that is going to be analyzed. Each detection has a particular number of expositions for the different EPIC cameras (some observations have several with each one of the three cameras, others only include one exposition, etc.) and also different exposure times. In order to simplify the analysis, for each observation only the expositions of the PN, MOS1 and MOS2 cameras with a larger exposure time have been considered, leaving all detections with a PN, MOS1 and MOS2 spectral file at most. Finally, the spectra is binned to allow one count as minimum per bin which is necessary in order to use the C-statistic (Cash, 1979).

After that, MOS spectra for an observation are merged by a script using HEASARC's *FTOOLS*[4] so an averaged spectrum is obtained, with as many counts as the sum of both spectra, a total exposure time and a new count rate. This merged spectrum has therefore a new background spectrum and a response file that are also created in the process. For sources with multiple observations all PN and MOS expositions are also merged, so a "merged" observation is created.

2.3 PyXspec and BXA

To analyse and model the spectra, tools to work with X-ray spectral data are needed. NASA's HEASARC (NASA/GSFC) provides useful software to manipulate FITS files (HEASoft package) as well as to fit the spectra to different models. PyXspec (Gordon and Arnaud, 2021) is a Python interface to the XSPEC (Arnaud, 1996) spectral-fitting program developed by Craig Gordon and Keith Arnaud (HEASARC Software Development) and is the software used in this work to perform the model fitting. The documentation is available at https://heasarc.gsfc.nasa.gov/xanadu/xspec/python/html/index.html.

When measuring the spectrum of a source the instrumental response must be taken into account. In this case, each spectral file containing the information of the number of counts detected per channel has associated to it a Redistribution Matrix Function (RMF) file (in units of cm^2) and a Auxiliary Response File (ARF) that are read by XSPEC as the detector response. The RMF comprises the information of the discrete function describing the probability of a photon of energy E being detected in a channel I through several energy ranges while the ARF represents the efficiency of the instrument.

For each spectrum there is as well an observed background spectrum needed to derive the background-subtracted spectra (in counts per second) by XSPEC. The next step is to define a model that should represent the actual spectrum of the source. This is calculated by XSPEC in the energy range defined by the response files and in units of $Photons\, cm^{-2}\, s^{-1}$. These three elements (measured spectra, the instrument response and model spectra) are the information needed to perform the spectral fitting. Before performing the spectral fitting, each individual spectrum is binned to a minimum of 1 count per bin in order to use W statistic, as described in Sect.2.3.2. To represent the fits, the *Plot* command in PyXspec permits us to get a plot of both the spectrum and the model, and additional information. For this work, we also plot the residuals of the fit and the unfolded spectrum and model

[4] https://heasarc.gsfc.nasa.gov/ftools/

in units of $Ef(E)$.

2.3.1 XSPECs Models

XSPEC offers a wide variety of model components with distinct characteristics. The models used to find the best fit to the X-ray emission of the studied AGN are presented in this section. All models include a multiplicative constant to account for the cross-normalization between the different EPIC instruments.

Simple Power-law

A first model is used to reproduce the continuum non-thermal X-ray emission that extends from 1 keV to 100 keV and that has a form of a power-law. In this case the hard band 2-10 keV (at the rest frame of each object) is considered. This model is defined as a simple power-law component, `zpowerlw` in XSPEC notation, convolved by a `clumin` component that allows us to calculate the luminosity of the power-law in a specified energy range. The model in XSPEC notation is given by "`clumin*zpowerlw`" and it has a total of 7 parameters:

- Four fixed parameters that consist of the redshift of the AGN, z, for both components; and the energy range (in the source frame) at which the luminosity of the power-law is going to be calculated, $E_{min} = 2.0\,keV$ and $E_{max} = 10.0\ keV$.
- The base 10 logarithm of the luminosity of the power-law given in $erg\,s^{-1}$. Typical values for the X-ray luminosity of type 1 AGN are $L \sim 10^{44}\,erg\,s^{-1}$. This is taken as the initial value for the fit and the parameter is free to vary between 10^{40} and $10^{47} erg\,s^{-1}$.
- The photon index of the power-law, Γ, defined in $A(E) = K[E(1+z)]^{-\Gamma}$. This is a free parameter that ranges from 0.1 to 4.0 with an initial value of $\Gamma = 2.0$
- The normalization of the power-law, fixed to $K = 1\,Photons\,keV^{-1}\,cm^{-2}\,s^{-1}$ as the `clumin` component is already being used.

Absorbed Power-law

The second model considers the whole energy range between 0.3-10 keV and introduces two new components that account for the absorption of the power-law. One of these components is `TBabs`, which corresponds to the Galactic absorption in the line of sight, while the other, `zTBabs` is used to model the intrinsic absorption of the AGN. This model ("`TBabs*zTBabs*clumin*zpowerlw`") has the following set of parameters:

- The equivalent hydrogen column density, N_H, for the `TBabs` component in units of $10^{22}\,cm^{-2}$ is a fixed value of the Galactic HI column density for each source measured by HI4PI (Bekhti et al., 2016). It can be calculated for the coordinates of an object using the gdpyc[5] python package.
- The redshift of the source, z.

[5] https://gdpyc.readthedocs.io/en/latest/#

- The intrinsic N_H of the source, in units of $10^{22}\,cm^{-2}$, is left as a free parameter of the fit from the `zTBabs` component. This parameter is set in an interval between $10^{19}\,cm^{-2}$ and $10^{24}\,cm^{-2}$ with an initial value of $N_H = 10^{21}\,cm^{-2}$.
- The rest of the parameters are identical to those of the previous model, corresponding to the `clumin` and `zpowerlw` components from which the luminosity and photon index of the power-law are obtained.

Absorbed Power-law with Black Body

For the third model, a black body component `zbbody` is added to reproduce the soft excess with respect to the hard X-ray continuum observed in a large fraction of AGN at energies below 2 keV, in the soft X-ray band. This black body spectrum considers the redshift of the object and has the following expression:

$$A(E) = \frac{K \times 8.0525[E(1+z)]^2 dE}{(1+z)(kT)^4[exp[E(1+z)/kT] - 1]} \tag{2}$$

In XSPEC notation, the model is written as `TBabs*zTBabs*(clumin*zbbody+clumin*zpowerlw)` where another `clumin` component is introduced to calculate the luminosity of the black body component in the soft band. The parameters of this model include the ones from the previous model corresponding to both the Galactic and intrinsic absorptions and the power-law profile. The new parameters for the black body component are:

- The fixed energy range at which the luminosity of the black body is calculated with the `clumin` convolution component is $E_{min} = 0.5\,keV$ and $E_{min} = 2.0\,keV$.
- The logarithm (base 10) of the luminosity associated to the black body is a free parameter taking an initial value of $10^{44}\,erg\,s^{-1}$ within the interval $10^{40} - 10^{47} erg\,s^{-1}$.
- The redshift of the source, z.
- The black body temperature, kT, is a free parameter that varies between $10^{-3}\,keV$ and $0.4\,keV$, with an initial value of $kT = 0.1\,keV$ based on the typical values found for the soft excess of $kT \sim 0.1 - 0.2\,keV$.
- The normalization (K) of the `zbbody` component is fixed and set to one in order to obtain its luminosity using `clumin`.

These are the base models used for this study, although additional models might be needed for sources with a more complex spectrum.

Double Power-law

For some sources, a single power-law is not enough to model the continuum, so an additional model with two power-laws is needed. The model is defined in a similar way as the absorbed power-law model, but now only one of the power-law components is absorbed while there is another component with no absorption, where a constant factor is added. The "double power-law" shape observed in the spectra of these AGN can arise due to different processes:

the absorbed AGN spectra could be contaminated by diffuse galactic emission, the presence of cold gas could be covering part of the power-law continuum emission or the light could be undergoing scattering from regions with different column densities (Winter et al., 2008). In XSPEC notation, the model is given by `cons*TBabs*(cons*clumin*zpowerlw + zTBabs*clumin*zpowerlw)`. The parameters are analogous to those used in the absorbed power-law as both `zpowerlw` components have their spectral index tied and the luminosities are calculated in the 2-10 keV energy range. The new `cons` component is a constant that varies from 0 to 0.2, as usually no more than the 10% of the power-law emission should be able to escape and be detected as unabsorbed.

2.3.2 Statistics in XSPEC

Statistics are used in two ways when performing a fit in XSPEC. First, to find the values of the parameters of the model that result in the best fit to the data, and their errors. This is parameter estimation, and it is usually done using the maximum likelihood as a statistic, so the best values of the parameters are those for which the probability of observing the data for a certain model is maximised (in practice, the used quantity is the log-likelihood, $l = -2lnP$). Then, after the fit is performed, the model and the best-fit parameters should be tested to see how accurately they fit the data. This second operation is known as the goodness of fit, and the χ^2 is the standard statistic used for it. A useful quantity is the reduced χ^2, defined as $\chi^2_{red} = \chi^2/dof$ where "dof" stands for the degrees of freedom (number of data bins minus the number of free parameters) and as a general guideline, it should be approximately equal to 1.

For CCD instruments and detectors that can make measurements of background spectra, the probability distribution underlying the data is considered to be a Poisson distribution. This has to be taken into account in the statistics of the fit. In the case of having Poisson distributions for the data and the background a combined likelihood is needed. This one will depend also on a model for the background data (C statistic), but modeling the background is of no interest for this work. The Profile Likelihood is calculated by finding the background count rate b_i for the best fit (for which the derivative of the likelihood will be zero) and is given by:

$$W/2 = \sum_{i=1}^{N} t_s m_i + (t_s + t_b) f_i - S_i ln(t_s m_i + t_s f_i) - B_i ln(t_b f_i) - S_i(1 - lnS_i) - B_i(1 - lnB_i) \quad (3)$$

where S_i are the observed counts, t_s and t_b the exposure times for the source and background spectra, m_i the predicted count rates, B_i the background data and $b_i = f_i$ is the background model. The expression for f_i is:

$$f_i = \frac{S_i + B_i - (t_s + t_b)m_i + d_i}{2(t_s + t_b)} \quad (4)$$

$$d_i = \sqrt{[(t_s + t_b)m_i - S_i - B_i]^2 + 4(t_s + t_b)B_i m_i} \quad (5)$$

Because some of the spectral data quality used in work, this W statistic is the one used instead of the C statistic (although is still labelled as "cstat") when introducing spectral data with an associated background spectrum file in XSPEC (Arnaud et al.), as it is discussed in the next section.

2.3.3 Bayesian statistics and BXA

The C-statistic and χ^2, however, present some problems when dealing with X-ray spectral analysis. The counts of extragalactic X-ray sources follow a Poisson distribution, making the C-statistic useful for parameter estimation as it is derived from a Poisson likelihood (as already mentioned in the previous section), but the χ^2 is still needed for testing the goodness of the fit. There are also difficulties when exploring the parameter space looking for the best-fit solution, as the commonly used optimization algorithms (e.g. Levenberg-Marquardt) are not able to identify local probability maxima. Error estimation can be problematic as well, relying on computationally costly simulations to avoid assuming gaussian probability distributions for the parameters.

A solution can be using a Bayesian approach, where each parameter is defined by the knowledge or assumptions made of it ("prior") and the result is a multivariate distribution of values referred to as "posterior".

Bayesian statistics is used for data analysis and parameter estimation and is based on Bayes theorem, which infers the probability of an hypothesis (model) being true conditioned by the observed evidence. This theorem can be expressed as:

$$P(M|D,I) = \frac{P(D|M,I)P(M,I)}{P(D,I)} \tag{6}$$

Where D is the data, M the model and I the previous information we might have; then $P(M,I)$ is the a priori probability of the model (known as the prior) and $P(D|M,I)$ the likelihood of the data. $P(M|D,I)$ is the a posteriori probability (posterior) given the observed data and $P(D,I)$ is referred to as the evidence for the model.

The probability of a set of values for the parameters θ_i given some data x_i is in general $P(\theta_1\theta_n|x_i) \propto P(x_i|\theta_1...\theta_n)P(\theta_1...\theta_n)$ and can be marginalised integrating (nowadays this can be done numerically) to get the probability of a particular parameter:

$$P(\theta_1|x_i) = \int d\theta_2 ... \int d\theta_n P(\theta_1...\theta_n|x_i) \tag{7}$$

An important part of the Bayesian inference method is the definition of the prior distributions that should be guided by previous information like empirical data or theoretical knowledge about the studied subject. For bounded parameters an uniform prior is typically used, but binomial, Poisson or Gaussian distributions for the priors are also common. Bayesian inference can also be applied to estimate probabilities for hypothesis tests such

as model comparison. Model selection using Bayesian statistics is done by comparing the evidence Z given by the integral over parameter space:

$$Z = \int \pi(\vec{\theta}) exp[-\frac{1}{2}C(\vec{\theta})] d\vec{\theta} \tag{8}$$

where the parameter vector $\vec{\theta}$ is weighted by the prior $\pi(\vec{\theta})$. The quantity $B_{12} = Z_1/Z_2$ is known as the Bayes factor and it quantifies how strongly one model should be preferred over the other one, using the Jeffreys scale (Jeffreys, 1961), the strength of evidence is "barely worth mentioning" for a factor 1-3, "substantial" for 3-10, "strong" for 10-30, "very strong" if >30 and "decisive" for a Bayes factor above 100.

In the case of X-ray spectral analysis, the posterior is given by Bayes theorem:

$$P(\vec{\theta}|D) = \frac{\pi(\vec{\theta}) P(D|\vec{\theta})}{Z(D)} \tag{9}$$

where $\pi(\vec{\theta})$ is the prior for a set of model parameters θ; $P(D|\theta)$ is the likelihood of the observed spectra, D, given a particular set of parameters and $Z(D)$ is the Bayesian evidence for the model.

One of the most common integration techniques used to explore the parameter space and find the values with higher probability is the Markov Chain Monte Carlo method (MCMC). This algorithm produces a new starting point in every iteration and it creates a chain with vectors for each parameter, whose length is proportional to its probability. Using MCMC it is also possible to find the errors for the parameters without assuming a normal distribution but the method presents some inconveniences, as it is a local algorithm with difficulty to find separated maxima.

A different Monte Carlo algorithm is Nested Sampling. In this case, the parameter space is scanned using parameter vectors of fixed size called "live points" and points with lower probability are replaced by those with higher likelihood in successive iterations.

Bayesian X-ray Analysis (BXA[6]) is a tool that allows the use of the Bayesian methods within PyXspec. This software package connects UltraNest[7], a library that carries out Bayesian analysis (parameter estimation and model comparison) using nested sampling algorithms, with PyXspec. UltraNest is able to calculate the posterior probability distribution for each parameter and the marginal likelihood ("evidence") Z. Apart from the posterior distributions, BXA also produces different files for each fit, such as corner plots as well as plots for the probability distributions, the chains of values explored and a summary with the results. It is therefore a useful tool for the analysis and modeling of X-ray spectra.

[6] http://johannesbuchner.github.io/BXA/
[7] https://johannesbuchner.github.io/UltraNest/

For analysing X-ray spectra, in this work we use the analysis software BXA (Buchner et al., 2014), which connects the nested sampling algorithm UltraNest (Buchner, 2021) with the fitting environment XSPEC (Arnaud, 1996). With these tools it is possible to combine the probability distributions of the results to infer sample distributions of some quantity. PosteriorStacker [8] is a python script developed by Johannes Buchner that allows deriving sample distributions from the posterior distributions of a number of objects. The method used is described in Baronchelli et al. (2020) and it computes the sample distribution using a histogram model and a Gaussian one. The outputs include a plot with both models and the UltraNest analysis output, as well as the posterior samples.

3 Results

3.1 Sample Selection

The catalogue used in this work that provides X-ray spectral data from XMM is 4XMM-DR12, a catalogue of serendipitous sources from overlapping observations that span across 21 years and gathers 939.270 detections (337.058 of them with available spectra) from 630347 unique sources, released in July 2022. The catalogue files as well as the documentation can be found on http://xmmssc.irap.omp.eu/Catalogue/4XMM-DR12/4XMM_DR12.html.

The crossmatching of the optical samples (described in Sect.2.1) has been carried out using the TOPCAT[9] tool (Taylor, 2005) and considering a maximum separation radius of 5 arcsec. In the case of crossmatches with multiple counterparts, a visual inspection of the X-ray object detected is made to ensure that the optical source corresponds to a unique X-ray source. For this, the 4XMM catalogue interface at https://xcatdb.unistra.fr/4xmmdr13/xcatindex.html has been used. After applying the filters explained in Sect.2, the match with the ZMS sample gives 399 observations of 186 sources while the one with the GAN sample gives 29 observations of 21 sources different from those on ZMS (3 sources were present in both samples).

This means that a 27.27% of the ZMS sample and a 5.92% of the GAN sample has been analyzed in this work. The low proportion of objects present in the crossmatch, especially in the case of the list of sources from GAN, is explained by the lack of observations made by XMM-Newton at their positions in the sky. Table 1 shows the number of sources from each sample that are within a 14 arcmin radius (approximately XMMs EPIC camera FOV) from the center of at least one observation, resulting in 198 sources from ZMS and 29 from GAN. Not all those objects can be studied as they must be not only observed, but individually detected and have measurements of their spectra. The proportion of sources that can be used is reduced to 28.59% (ZMS) and 7.04% (GAN) as a result. Nevertheless, the number of detected objects with respect to the observed ones is rather high for both samples (98.99% for ZMS and 96.55% for GAN). From those, 186 sources from ZMS (27.27% of the total)

[8] https://github.com/JohannesBuchner/PosteriorStacker/tree/main
[9] https://www.star.bristol.ac.uk/mbt/topcat/

	Num. of Sources in the sample	Sources observed by XMM (%)	Sources with detections (%)	Sources detected with spectra (%)	analyzed sources (%)
ZMS	682	198 (29.03%)	196 (28.73%)	195 (28.59%)	186 (27.27%)
GAN	355	29 (8.17%)	28 (7.89%)	25 (7.04%)	21 (5.92%)

Table 1: Comparison of the ZMS and GAN samples and observations made by XMM-Newton showing the proportion of objects that have been observed, those that are observed and detected, the sources detected with available spectra and finally the number of sources analyzed in this work after applying the quality filters explained in 2.2.2 (% with respect to the total number of sources in the original sample).

and 21 from GAN (5.92%) remain after taking into account the quality filters explained in Sect.2.2.2. The proportion of analyzed sources with respect to those with spectra is therefore 95% for ZMS and 84% for GAN, this is not a significant difference as many GAN objects have not been observed by XMM and have higher redshift.

XMM crossmatched sample	Sources	Observations	Sources with multiple obs.
GAN	21	29	7
ZMS	186	399	87
Total	207	508	94

Table 2: Final summary of analyzed sources and observations from the two used data samples.

The final list of objects comprises 508 observations of 207 sources, with values of redshift in a range from $z = 0.0039$ to $z = 0.9499$. Table 2 presents the final number of objects that have been analyzed, the total number of observations and the number of sources with several observations for each sample.

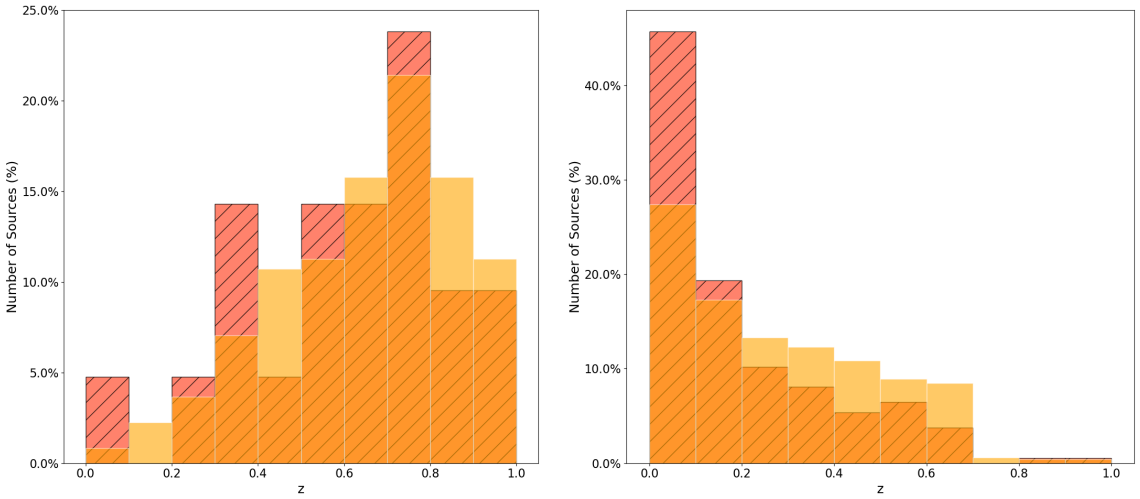

(a) (b)

Figure 5: Redshift histograms of the analyzed data samples (yellow): GAN (a) and ZMS (b), along with the sub-sample obtained in the crossmatch with the XMM catalogue for this work (red hatched bars).

In Figure 5, the distributions of redshift of both the original sample and the resulting crossmatch are shown. The analyzed sample is representative of the GAN and ZMS data as no selection bias in the redshift can be appreciated.

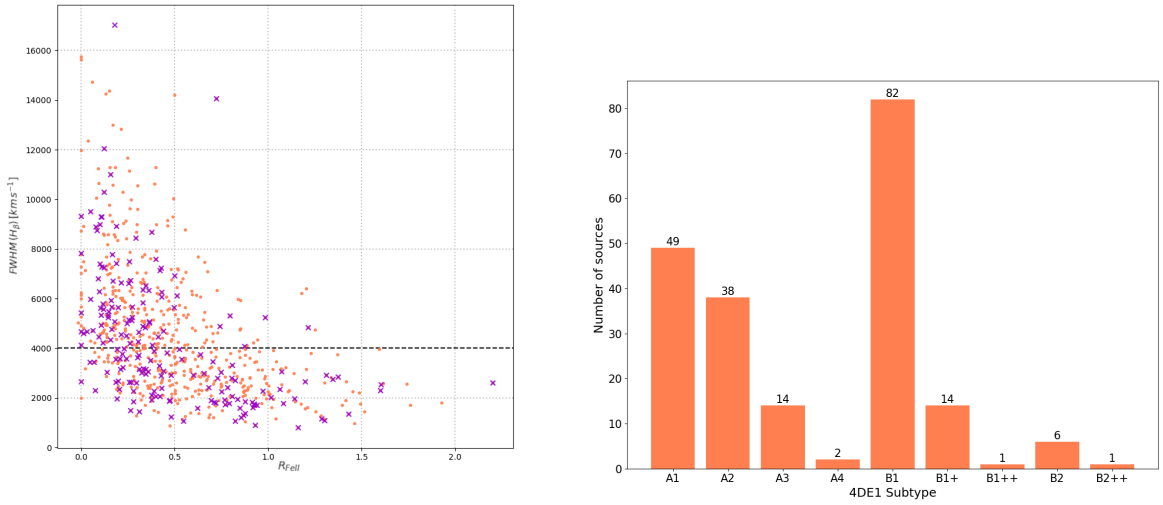

(a) (b)

Figure 6: Optical plane of the main sequence (FWHM(Hβ) against R_{FeII}) for ZMS sample (red points) and the sample studied in this work resulting from the crossmatch with the XMM catalogue (purple crosses)(a) and total number of sources by spectral sub-type (b).

As one of the objectives of this work is to study the properties of the X-ray emission of quasars depending on their spectral type, it is important for the sample to include objects of different populations. This means that the studied sample should be evenly distributed along the main sequence so that there is a significant number of objects of the different subtypes. This is shown in Figure 6a for the ZMS sample, where it can be seen that the crossmatch does not introduce any bias in this regard. In Figure 6b the total number of sources by spectral sub-type (following the 4DE1 eigenvector formalism described in Sect.1.2) is shown.

The most numerous types are B1 and A1, while there are fewer objects of the types at the extremes of the main sequence (i.e. A4 and B++).

A detailed list of the number of sources for each sub-type, divided by data sample, is shown in Table 3. There are a total of 103 objects from Population A and 104 from Population B, making the analyzed objects a good sample to compare the properties of both populations.

3.2 X-ray Spectral Analysis

In Sect.2.2 it was already mentioned how the X-ray spectral data were selected to leave only one data set per object, as multiple observations of the same object and EPIC camera (pn or MOS) were merged to have an averaged spectrum.

Spectral Type	Num. of sources (ZMS)	Num. of sources (GAN)	Total
A1	48	1	49
A2	37	1	38
A3	14	0	14
A4	2	0	2
B1	66	16	82
B1+	13	1	14
B1++	0	1	1
B2	5	1	6
B2++	1	0	1

Table 3: Distribution of spectral sub-types in the 4DE1 formalism by data sample.

By doing this, every fit will be simultaneously done to a maximum of 2 spectra (one for the PN camera and other for the merged MOS1+MOS2) per source. A total of 94 objects (Table 2) have multiple observations that have been averaged, permitting a complete analysis of the source without choosing one observation over another.

In addition to the 207 fits corresponding to 113 sources with a unique observation and 94 sources with merged observations, all the remaining spectra has also been fitted using the BXA tool in PyXspec (a total of 602 spectral fittings) in order to evaluate source spectral variability when necessary. The models used to fit the data are explained in Sect.2.3.1.

3.2.1 Simple Power-law

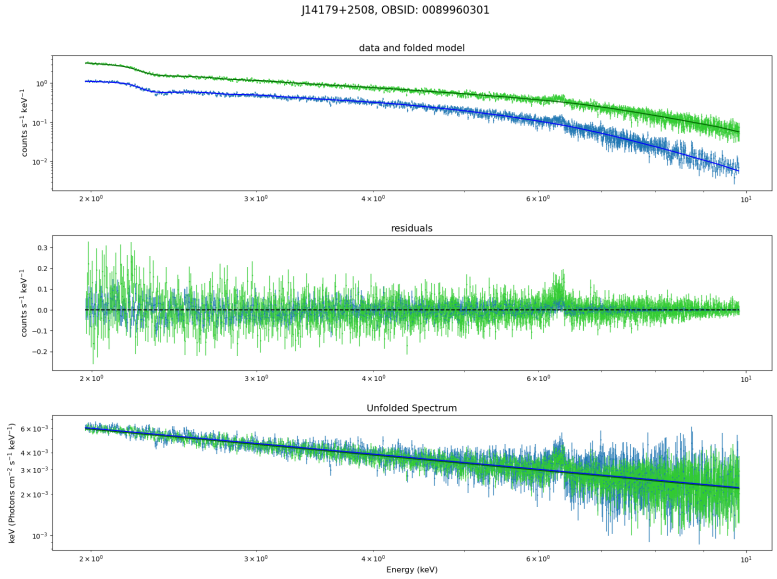

Figure 7: Example of a fit to the simple power-law model (`clumin*zpowerlw`)performed using BXA and PyXspec. The first plot represents the spectrum measured by the PN and MOS instruments (green and blue) and the fitted model (green and blue lines). The residuals of the fit are shown in the middle plot and the unfolded spectrum and model are plotted in the third one.

For the first model, only the counts in the band 2-10 keV (rest frame) are considered, in order to fit a simple power-law without taking into account the soft X-ray band. The priors for the parameters that define the power-law (the photon index Γ, and its luminosity) are defined using the tool BXA. For both the luminosity and photon index parameters the priors are uniform in the ranges specified in Sect.2.3.1, while for the cross-calibration constant (for sources with spectra from the PN and MOS instruments) a logarithmic uniform prior is used. The priors chosen must be uniform in order to use the *PosteriorStacker* software script and obtain the combined probability distributions for the different populations. Using PyXspec we are able to plot both the data and the fitted model, as shown in Figure 7.

Figure 8 is presented as an example of the corner plots and the posterior distributions produced by BXA for each parameter. The median of the posterior distributions is shown hereinafter as the resulting value of the fit for each parameter in the following figures.

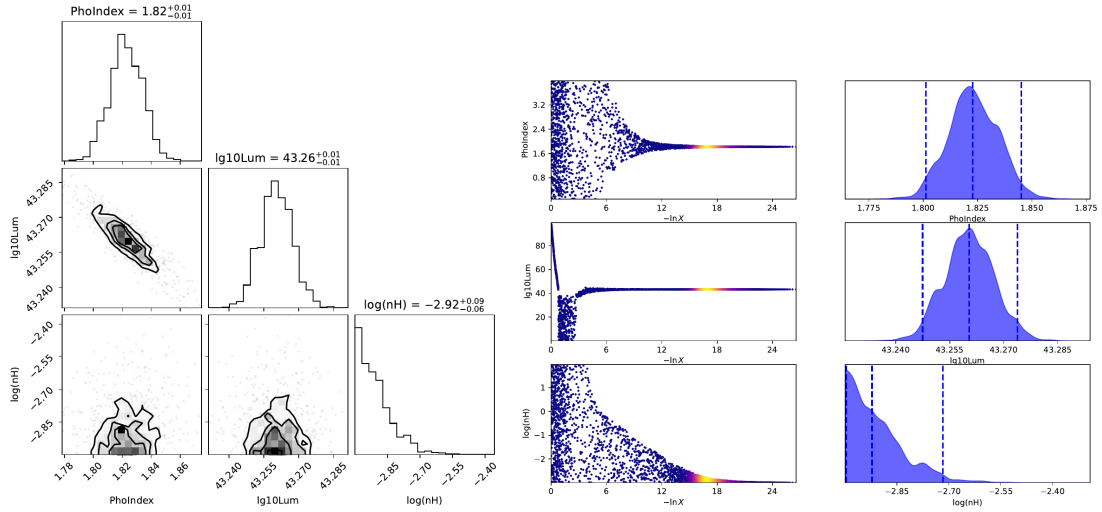

(a) (b)

Figure 8: Example of some of the outputs generated by BXA from a fit to the absorbed power-law model. Left: Corner plot where the given values for the parameters are the median with errors corresponding to the 16% and 84% quantiles; Right: Trace plots. In the posterior distributions the dashed lines correspond to the median value and the 2.5% and 97.5% quantiles.

In order to study the differences in the X-ray properties between the different types of sources the results have been analyzed separating the two populations of quasars, A (high accretion rate) and B (low accretion rate). In Figure 9 the results obtained for the photon index are presented for the 207 studied objects, along with the median value of both distributions.

The values of the photon index for Population A and B seem to follow different distributions, with sources of type A having a higher median ($\Gamma = 1.86$) than those of type B ($\Gamma = 1.69$). A Kolmogórov-Smirnov (K-S) test supports the idea of the distributions being different as the p-value is of the order of 10^{-7}. Although the results concentrate between $\Gamma = 1$ and $\Gamma = 2.5$ both distributions also show a tail of low values for the photon index

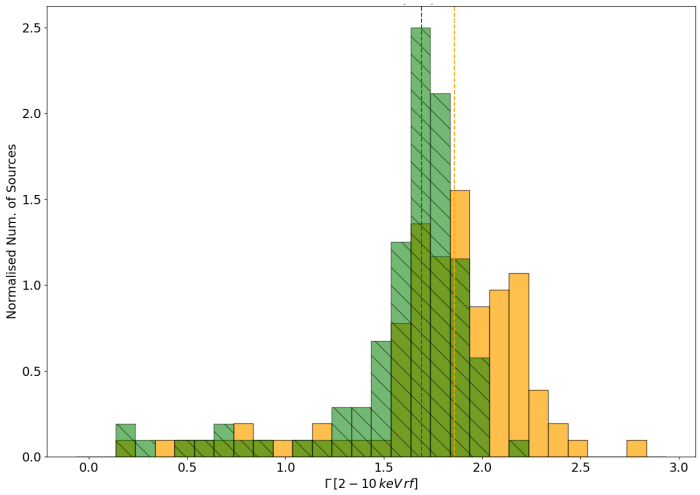

Figure 9: Photon index (Γ) obtained for the fit to the simple power-law model in the [2-10 keV] (rest frame) band. Sources of Population A are displayed in yellow and Population B in green, along with dashed lines representing the median Γ value of each population: $Med(A) = 1.86$, $Med(B) = 1.69$. K-S test p-value $p = 9.10 \cdot 10^{-7}$.

that are not physical. A more complex model is needed to reproduce the spectral shape of these sources, as it is addressed in the following sections.

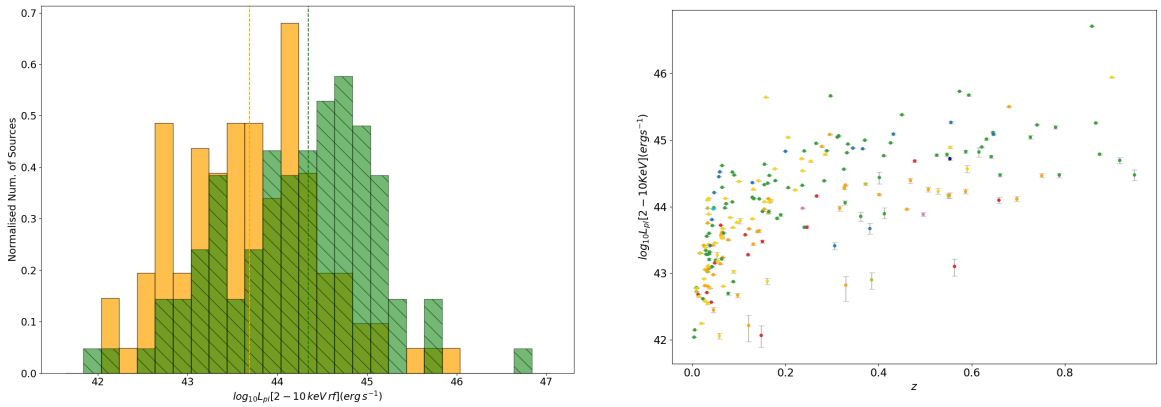

(a) (b)

Figure 10: Left: Power-law luminosity ($log_{10}L_{pl}[2-10keV]\,(erg\,s^{-1})$) obtained for the fit to the simple power-law model in the [2-10 keV] (rest frame) band. Sources of Population A are displayed in yellow and Population B in green, along with dashed lines representing the median $log_{10}L_{pl}\,(erg\,s^{-1})$ value of each population: $Med(A) = 43.69$, $Med(B) = 44.35$. K-S test p-value $p = 9.84 \cdot 10^{-7}$. Right: Power-law luminosity ($log_{10}L_{pl}\,(erg\,s^{-1})$) against the redshift (z) of all sources colored by spectral sub-type: A1 (yellow), A2 (orange), A3 (red), A4 (pink), B1 (green), B1+ (blue), B1++ (navy), B2 (olive) and B2++ (cyan). Error bars correspond to the 16% and 84% quantiles.

The luminosity of the power-law can be calculated using the `clumin` component as explained in Sect.2.3.1. Analogously to the previous case, the results are displayed in the

form of an histogram in Figure 10a.

With these values of luminosity we can also characterize the sample by plotting the results obtained in the fitting process against the redshift. This redshift - luminosity diagram is shown in Figure 10b, where each point corresponds to a source, colored by its spectral sub-type and with error bars defined by the 34.1% percentiles (equivalent to the 1 sigma interval for normal distributions) of the posterior distributions.

3.2.2 Absorbed Power-law

The next step is to consider also the soft X-ray emission, adding the components to the model that account for both the Galactic and intrinsic absorption. In Figure 11 an example of a fit for this model is presented, now considering all the data between 0.3 and 10 keV.

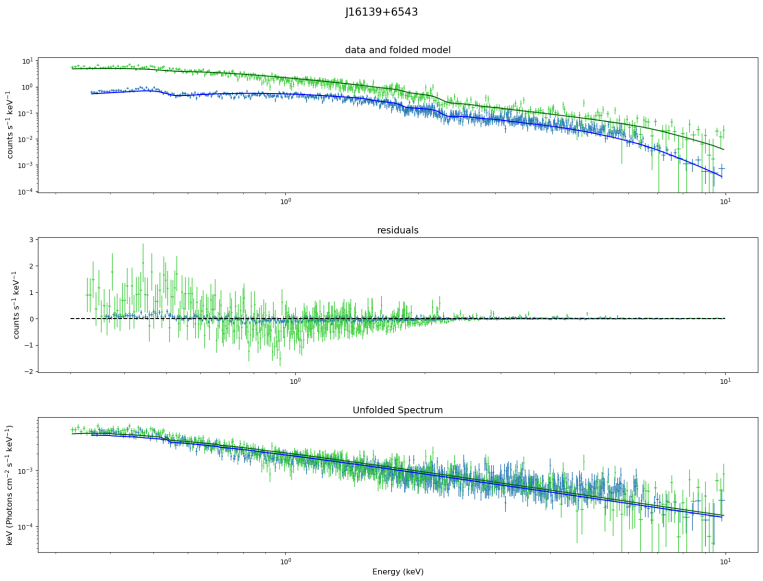

Figure 11: Example of a fit to the absorbed power-law model (`TBabs*zTBabs*clumin*zpowerlw`) performed using BXA and PyXspec. The first plot represents the spectrum measured by the PN and MOS instruments (green and blue) and the fitted model. The residuals of the fit are shown in the middle plot and the unfolded spectrum and model are plotted in the third one.

Analogously to the previous model, the luminosity of the power-law obtained from the posterior distributions of each source is presented in a histogram separating the two quasar populations.

As it can be seen on Figure 12, the results are similar to the ones obtained with the simple power-law model. Population B objects are more luminous and the distributions are significantly different as indicated by the K-S test p-value with a value of $\sim 10^{-6}$.

In the case of the photon index, the differences between the two populations become more evident after including the soft X-ray emission. The histogram with the results for all sources is shown in Figure 13. Population A objects show a greater median for this parameter, $\Gamma = 2.34$, while the value is $\Gamma = 1.97$ for Population B, a difference between

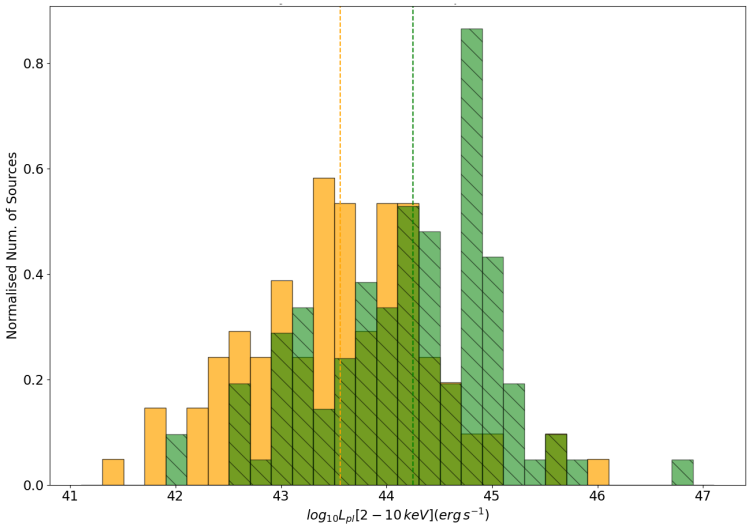

Figure 12: Power-law luminosity ($log_{10}L_{pl}[2-10keV]\,(erg\,s^{-1})$) obtained for the fit to the absorbed power-law model in the [0.3-10 keV] band. Sources of Population A are displayed in yellow and Population B in green, along with dashed lines representing the median $log_{10}L_{pl}\,(erg\,s^{-1})$ value of each population: $Med(A) = 43.56$, $Med(B) = 44.25$. K-S test p-value $p = 2.11 \cdot 10^{-6}$.

the two values that has increased from 0.17 to 0.37 with respect to the previous model. The visual difference between populations, with type B objects being more concentrated around $\Gamma \approx 2$ while type A extend beyond $\Gamma \approx 2.5$ is statistically confirmed by the K-S test p-value of the order of $\sim 10^{-12}$.

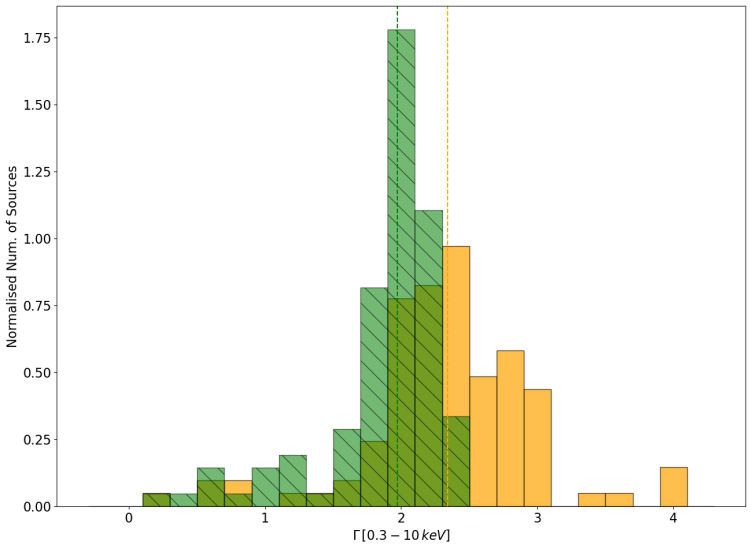

Figure 13: Photon index (Γ) obtained for the fit to the absorbed power-law model in the [0.3-10 keV] band. Sources of Population A are displayed in yellow and Population B in green, along with dashed lines representing the median Γ value of each population: : $Med(A) = 2.34$, $Med(B) = 1.97$. K-S test p-value $p = 5.07 \cdot 10^{-12}$

The distributions also show some similarities. One is the tail of values below $\Gamma \approx 1.5$ that corresponds to objects which need a different analysis, and the other is the fact that for both populations the median photon index has increased after taking into account the emission between 0.3-2 keV.

To better visualize how the photon index changes when considering the soft emission, in Figure 14 $\Gamma[0.3-10\,keV]$ from the simple power-law model is plotted against $\Gamma[2-10\,keV]$ obtained fitting the spectra with the absorbed power-law model. As it was shown in the histogram, points representing sources of Population A (mainly A1, A2 and A3) have higher values of photon index, but they are also situated farther above the diagonal (dashed line in the plot). This means that they have a larger photon index with respect to the hard photon index in the [2-10 keV] band due to the soft emission of the object.

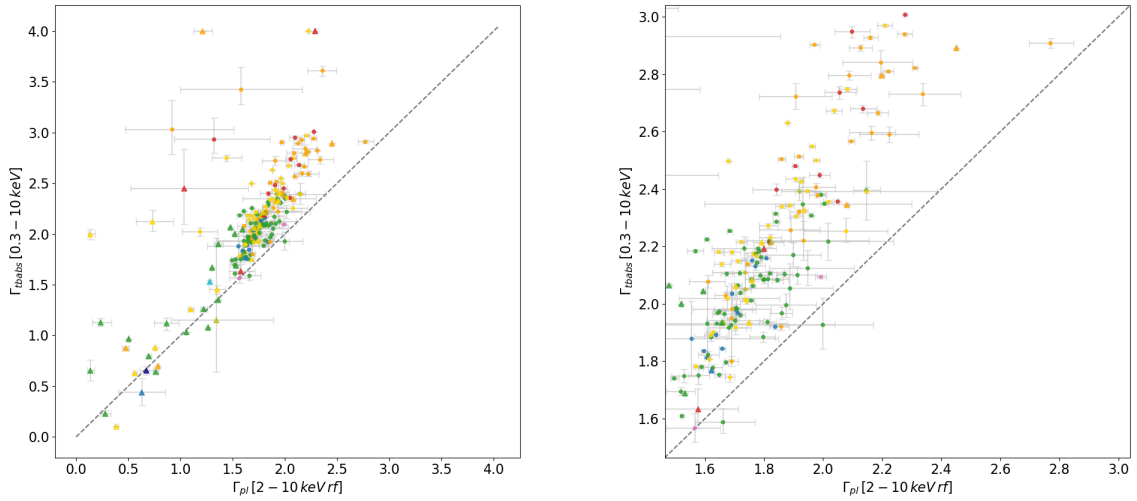

(a) (b) Detail of the plot

Figure 14: Photon index from the absorbed power-law model ($\Gamma_{tbabs}[0.3-10keV]$) against the photon index from the simple power-law model ($\Gamma_{pl}[2-10keV]$). The spectral sub-types are presented here as: A1 (yellow), A2 (orange), A3 (red), A4 (pink), B1 (green), B1+ (blue), B1++ (navy), B2 (olive) and B2++ (cyan). Triangles represent sources that need a different analysis (double power-law) and error bars correspond to the 16% and 84% quantiles for both parameters. The gray dashed diagonal represents the y=x line.

There are some outliers as well in the plot that are worth mentioning. Points represented with triangles are sources that cannot be described using the absorbed power-law model and need a different analysis (like a double power-law), which explains the existence of all the sources with $\Gamma < 1.5$ in the presented data. There are also some sources with a high photon index $\Gamma[0.3-10\,keV] > 3.5$ that present a strong soft emission (soft excess) and two objects with $\Gamma[0.3-10\,keV] \approx 3$ but a photon index $\Gamma[2-10\,keV] < 1.5$ that have a low number of counts, which could produce unreliable results.

After fitting this model and studying the shape of the residuals, it is clear that there are objects which need a more complex model for their spectrum. That will be either an

absorbed power-law with a black-body component to reproduce the soft X-ray emission or a double power-law, as it will be described in the following sections.

3.2.3 Absorbed Power-law with Black Body

Although for some objects the absorbed power-law model may be sufficient to describe their spectrum, this model with a black-body component is fitted to all sources in order to quantify their soft excess, since as it can be seen in Figure 14 many of them do present some soft excess to a greater or lesser extent.

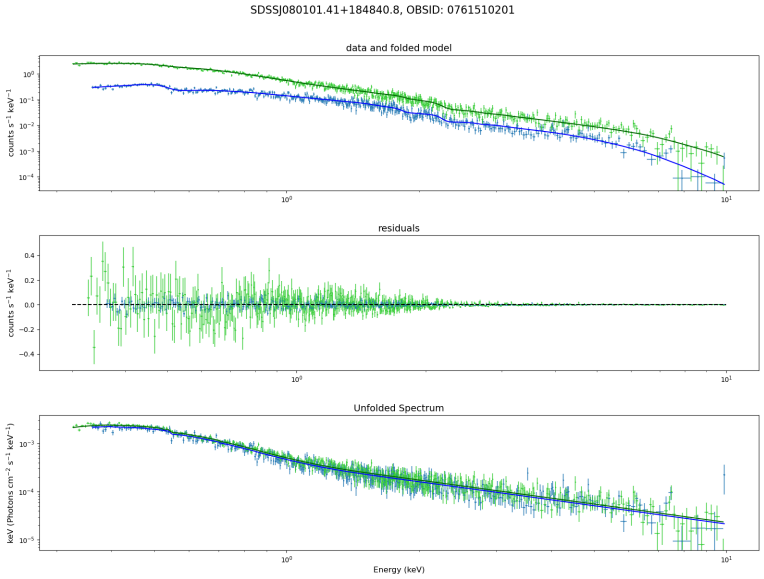

Figure 15: Example of a fit to the absorbed power-law with black-body (`TBabs*zTBabs*(clumin*zbbody+clumin*zpowerlw)`) performed using BXA and PyXspec. The first plot represents the spectrum measured by the PN and MOS instruments (green and blue) and the fitted model. The residuals of the fit are shown in the middle plot and the unfolded spectrum and model are plotted in the third one.

An example of a fit to the black-body model is shown in Figure 15 , where the significant soft emission above the power-law is visible. As in the previous cases, the median value of the posterior distribution for different parameters is calculated and presented in histograms.

The values of the power-law luminosity for this model are shown in Figure 16. As expected, the results are in accord with the ones from simpler models with objects of Population B being more luminous than those of Population A (median $log_{10}L_{pl} = 44.25 erg\, s^{-1}$ and $log_{10}L_{pl} = 43.56 erg\, s^{-1}$ respectively) and the distributions being statistically different with a p-value for the K-S test of $\sim 10^{-6}$.

The histogram in Figure 17 presents the results of the photon index for all sources, including those needing a different analysis and hence the tails of the distributions below $\Gamma = 1$.

Introducing the black-body component results in the values of the photon index decreasing with respect to the results of the previous model. Quasars of Population A now have a

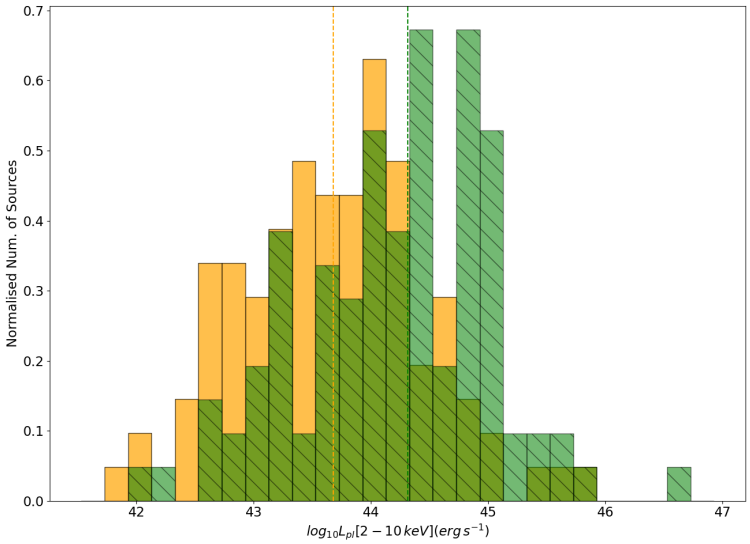

Figure 16: Power-law luminosity ($log_{10}L_{pl}[2-10keV]\,(erg\,s^{-1})$) obtained for the fit to the absorbed power-law with black-body model in the [0.3-10 keV] band. Sources of Population A are displayed in yellow and Population B in green, along with dashed lines representing the median $log_{10}L_{pl}\,(erg\,s^{-1})$ value of each population: $Med(A) = 43.68$, $Med(B) = 44.31$. K-S test p-value $p = 1.82 \cdot 10^{-5}$.

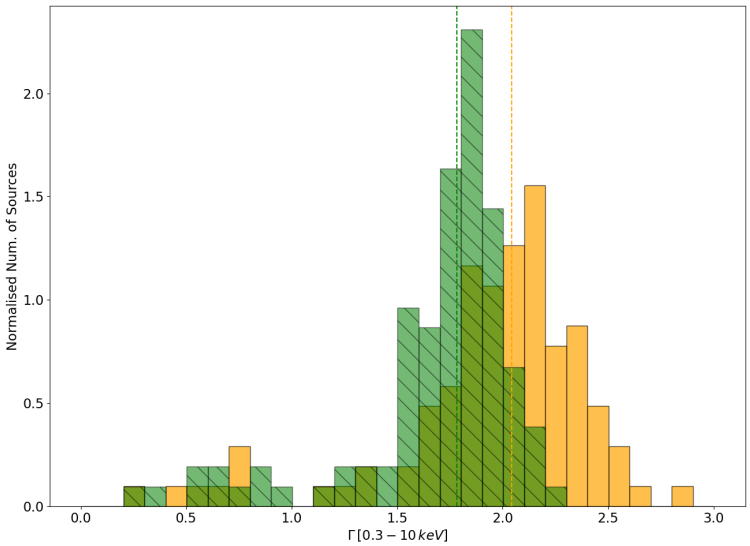

Figure 17: Photon index (Γ) obtained for the fit to the absorbed power-law with black-body model in the [0.3-10 keV] band. Sources of Population A are displayed in yellow and Population B in green, along with dashed lines representing the median Γ value of each population: $Med(A) = 2.04$, $Med(B) = 1.78$. K-S test p-value $p = 3.30 \cdot 10^{-10}$.

median $\Gamma = 2.04$ while the value for type B sources is $\Gamma = 1.78$. The difference between the distributions are confirmed again with a K-S test p-value of $\sim 10^{-5}$ and their distinct shapes: type A objects follow a more extended distribution while the Population B distribution seems to be more concentrated around a value of the photon index.

Another interesting result is comparing the values of Γ before and after introducing the black-body component to model a possible soft-excess. In Figure 18 Γ_{bb} is plotted against Γ_{tbabs} for the 160 sources for which this model is an acceptable fit.

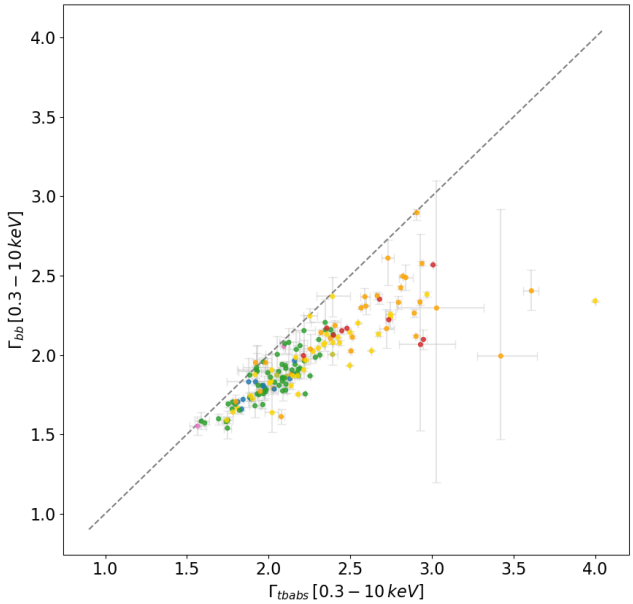

Figure 18: Photon index from the absorbed model with black-body ($\Gamma_{bb}[0.3-10keV]$) against the photon index from the absorbed power-law model ($\Gamma_{tbabs}[0.3-10keV]$). The spectral sub-types of the 160 sources are presented here as: A1 (yellow), A2 (orange), A3 (red), A4 (pink), B1 (green), B1+ (blue) and B2 (olive). Error bars correspond to the 16% and 84% quantiles of both parameters and the gray dashed diagonal represents the y=x line.

The main feature of the plot that can be observed is that objects of type B have lower photon index and are closer to the diagonal, while Population A sources move farther to the right.

3.2.4 Double Power-law

When analysing the results for the photon index parameter of the three models we encounter values below $\Gamma \approx 1.5$ that make no physical sense.

As AGN are complex objects it is possible that some of the studied sources needed a different model than the ones initially applied. After carrying out a visual inspection of all the spectra of these sources with anomalous results, 47 of them were identified as objects with a double power-law-like profile, and a new fit was performed for all of them.

In Figure 19 an example of a fit to the double power-law model described in Sect.2.3.1 is shown. The spectrum shows a characteristic shape where a portion of the power-law is absorbed.

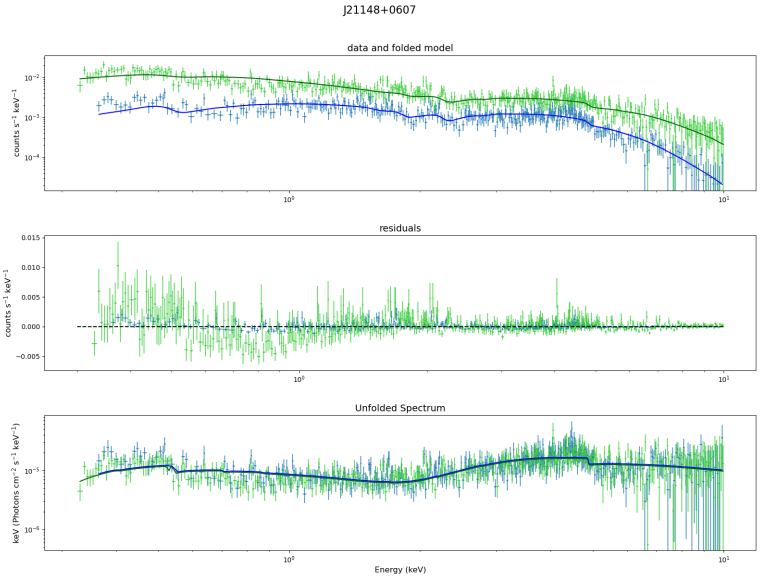

Figure 19: Example of a fit to the absorbed power-law model (`cons*TBabs*(cons*clumin*zpowerlw + zTBabs*clumin*zpowerlw)`) performed using BXA and PyXspec. The first plot represents the spectrum measured by the PN and MOS instruments (green and blue) and the fitted model. The residuals of the fit are shown in the middle plot and the unfolded spectrum and model are plotted in the third one.

For many of these objects (30 out of 47), nevertheless, a double power-law is not enough to model their spectra and more complex models including additional thermal emission or ionized absorption may be needed, which is beyond the scope of the current work. They are therefore excluded from the final analysis of the results in the following sections.

For the 17 for which the double power-law is an acceptable model we find that the resulting Γ tends to be higher for Population A, and therefore the differences between populations seem to hold also for this model.

3.2.5 Best-fit model

To determine which model, among the three used in this work, better represent the spectral shape in each case, a model comparison can be made using Bayesian methods.

Best-fit model	Number of sources
Absorbed power-law	19/207
Absorbed power-law with blackbody	141/207
Double power-law	17/207
Different model (variable, apec, etc)	30/207

Table 4: Number of sources that prefer each model given by the ModelCompare tool. "Different model" refers to sources that need a more complex and individual analysis.

In this case, the python software ModelCompare[10] developed by Johannes Buchner has

[10] https://github.com/JohannesBuchner/BXA/blob/master/examples/xspec/model_compare.py

been used to carry out the analysis. This tool uses the Bayesian evidence of the fits to compare different models and conclude which ones can be ruled out or not, based on a threshold given by a Bayes factor Z=100 (see Sect.2.3.3). The result of this analysis is presented in Table 4.

Based on the Bayes factor, the following results consider the best fit for each of the 160 sources for which a reliable analysis of the soft emission can be made. Of this new subsample, 81 objects are of Population A while the other 79 are Population B quasars. The other 47 sources (22 of Population A, 25 of Population B) need other models like the double power-law or more complex ones to account for their individual properties. For 30 of these 47 sources the statistically best fit would be the model with black-body, but a visual study of the residuals of each source reveals that the do not present a soft excess and applying a black-body component to them is therefore not justified in terms of the physical phenomena we are studying. When presenting the results of the best fit, the values for the power-law luminosity and its photon index correspond to the absorbed power-law model with black-body unless the absorbed power-law model is not statistically ruled out.

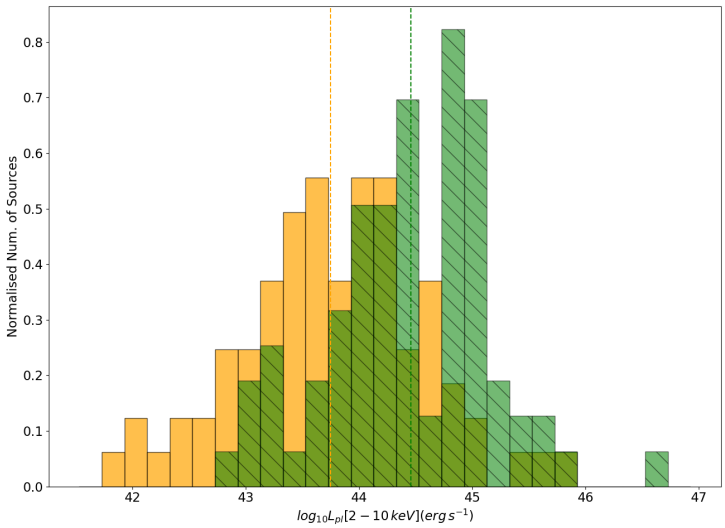

Figure 20: Power-law luminosity ($log_{10}L_{pl}[2-10keV]\,(erg\,s^{-1})$) obtained for the best fit (absorbed model with or without black-body). Sources of Population A are displayed in yellow and Population B in green, along with dashed lines representing the median $log_{10}L_{pl}\,(erg\,s^{-1})$ value of each population: $Med(A) = 43.75$, $Med(B) = 44.46$. K-S test p-value $p = 3.42 \cdot 10^{-6}$.

In Figure 20 the values for the power-law luminosity are presented. As it has been already pointed out by previous results, we find that quasars of Population B tend to have a higher luminosity than those of Population A. The median values of the distributions, represented by dashed lines, are $log_{10}L_{pl} = 43.75 erg\,s^{-1}$ for type A objects and $log_{10}L_{pl} = 44.46 erg\,s^{-1}$ for type B.

The results for the photon index are presented in Figure 21. Unlike the previous histograms where a tail of low, non-physical Γ values was present, for the remaining 160 objects, there are no values below $\Gamma \approx 1.5$. The distributions also confirm the already observed difference

between the two populations of quasars, also given by the K-S test p-value, $p \sim 10^{-11}$. Type A objects have a steeper power-law profile with a median of $\Gamma = 2.11$ while the value for type B objects is $\Gamma = 1.86$.

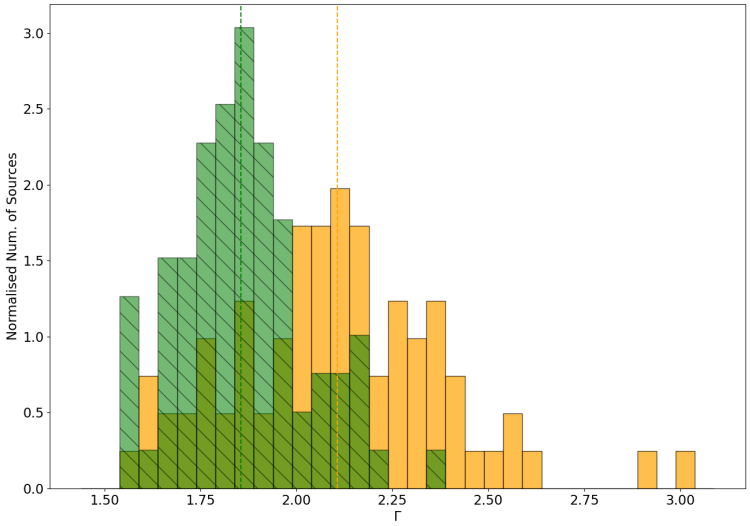

Figure 21: Photon index (Γ) obtained for the best fit (absorbed model with or without black-body). Sources of Population A are displayed in yellow and Population B in green, along with dashed lines representing the median Γ value of each population: $Med(A) = 2.11$, $Med(B) = 1.86$. K-S test p-value $p = 9.43 \cdot 10^{-11}$

3.3 Well-studied and variable sources

For a number of sources, an acceptable fit has not been found. Studying the cases individually revealed that these were objects with several observations. When merging the different observations an averaged spectrum is obtained, but if the object is a variable source, then the resulting spectra may not be reliable. A visual study of the fits of the individual observations revealed some variable sources that have been observed on multiple occasions by XMM and whose spectra show significant differences depending on the observation.

Name	Num. of obs.	Previous studies
J10235+1951 (NGC 3227)	6	Newman et al. (2021), Wang et al. (2022)
J11067+7234 (NGC 3516)	6	Mehdipour et al. (2010)
SDSSJ111706.40+441333.3 (PG 1114+445)	11	Serafinelli et al. (2021)
J14179+2508 (NGC 5548)	18	Cappi et al. (2016)
J18421+7946 (3C 390.3)	2	Gliozzi et al. (2009), Popovic et al. (2011)
J20441-1043 (Mrk 509)	16	Kumari et al. (2021)

Table 5: List of sources identified as variable by analysing the fits of the different observations and a reference to an in-depth study of each one.

The sources presented in Table 5 have been identified as variable and, furthermore, they are well-known QSO that have been the subject of studies by other authors.

One can find in the literature in-depth studies of these objects and their variability, with more complex models that are able to characterize their properties more accurately. In Table 5 some example papers of each source are mentioned.

4 Discussion

4.1 Hard (2-10 keV) photon index

A simple power-law in the 2-10 keV energy range has been fitted to the whole sample, allowing us to study the distribution of this parameter in an uniform way.

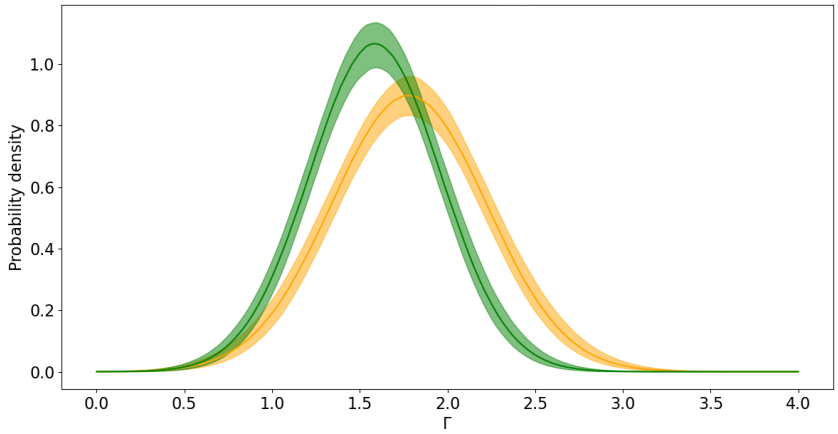

Figure 22: Sample probability distributions for the photon index (Γ) in the [2-10 keV] (rest frame) band following the Gaussian model computed using PosteriorStacker. Population A displayed in yellow and B in green with error bands corresponding to the 1-sigma interval. Mean and standard deviation of each curve are: $\mu = 1.78$, $\sigma = 0.45$ (A) and $\mu = 1.59$, $\sigma = 0.38$ (B).

Figure 22 shows the probability distributions of the photon index for both populations following a Gaussian model as computed by PosteriorStacker. These distributions are therefore characterized by a mean value and a standard deviation, as indicated in Figure 22. The inferred probability distributions are in accord with the histogram showing that objects of Population A have a higher mean photon index ($\Gamma = 1.78$) than those of Population B ($\Gamma = 1.59$) in the hard X-ray band.

Using PosteriorStacker it is also possible to compute the sample distributions of this parameter separating the different sub-types of the quasar main sequence. This is shown in Figure 23 where the Gaussian distributions of objects of types A1, A2, xA (extreme Population A including A3 and A4), B (types B1 and B2) and B+ (including B and B++) are presented.

The largest mean value for the photon index is that of the sub-type A2 with $\Gamma = 1.93$ while the lowest corresponds to objects of sub-types B+ with $\Gamma = 1.54$. Between them,

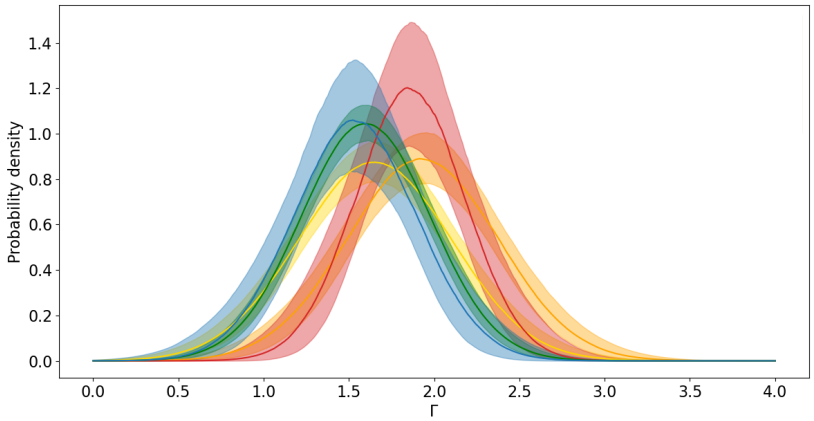

Figure 23: Sample probability distributions for the photon index (Γ) in the [2-10 keV] (rest frame) band following the Gaussian model computed using PosteriorStacker. The population subtypes presented are B+ (blue), B (green), A1 (yellow), A2 (orange) and xA (red) with error bands corresponding to the 1-sigma interval. Mean and standard deviation of each curve are: $\mu = 1.54$ and $\sigma = 0.38$ (B+); $\mu = 1.60$, $\sigma = 0.38$ (B); $\mu = 1.65$, $\sigma = 0.46$ (A1); $\mu = 1.93$, $\sigma = 0.45$ (A2) and $\mu = 1.86$, $\sigma = 0.33$ (xA).

sub-types A1 and B also show a flatter index ($\Gamma = 1.65$ and $\Gamma = 1.60$ respectively) while extreme Population A objects (xA) have a steeper profile ($\Gamma = 1.86$).

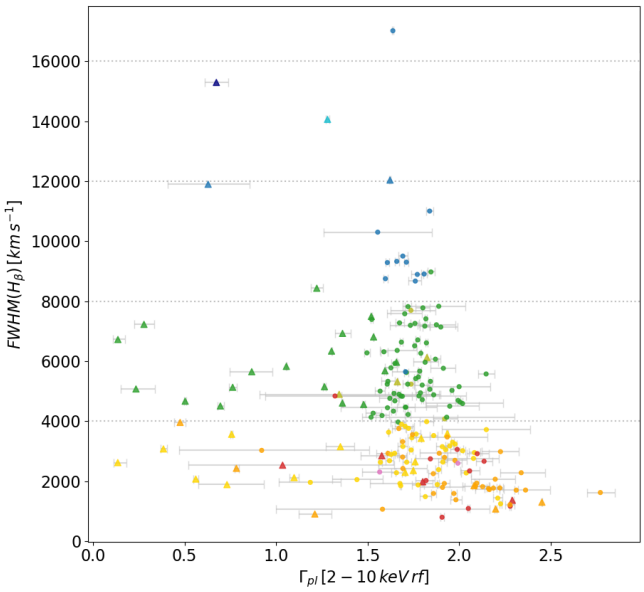

Figure 24: FWHM(Hβ) against the photon index [2-10 keV] from the simple power-law model (Γ_{pl}). All spectral sub-types are presented here: A1 (yellow), A2 (orange), A3 (red), A4 (pink), B1 (green), B1+ (blue), B1++ (navy), B2 (olive) and B2++ (cyan). Triangles represent sources that need a different analysis (double power-law) and error bars correspond to the 16% and 84% quantiles.

The fact that the X-ray photon index obtained by fitting a simple power-law model becomes lower as we move from Population A to Population B could be related to the optical plane of the main sequence (MS) where sub-types B+ and xA are positioned at opposite ends of the distribution (e.g. Figure 3).

In Figure 24 the photon index of each one of the 207 sources is represented against the FWHM(Hβ) parameter. Triangles designate objects with a non-physical photon index value and whose spectra need to be fitted using a double power-law model. We can see that there is a tendency for the photon index to increase for sources of Population A, and especially extreme accretors (A2 and A3).

4.2 Best-fit photon index

An acceptable fit has been found for 177 out of 207 sources by using one of the three models considered in this work: an absorbed power-law, a power-law with a black body, and a double power-law.

To study the distribution of the photon index of the sample, we derived the probability distributions of this parameter for each population using PosteriorStacker. In Figure 25 the distributions of the photon index are presented. The difference between the two populations is clear, with type B objects showing a distribution with mean $\mu = 1.86$ and a higher probability density which translates in a standard deviation $\sigma = 0.16$. Population A, on the other hand, presents a wider distribution with mean $\mu = 2.10$ and $\sigma = 0.27$.

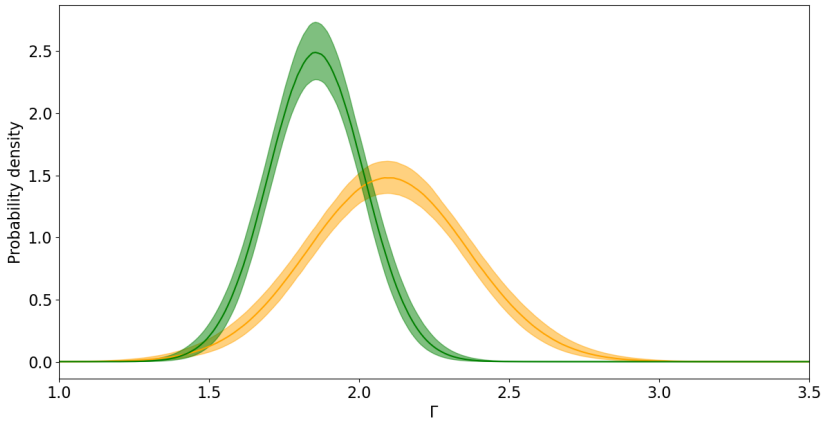

Figure 25: Sample probability distributions for the photon index (Γ) of the best fit following the Gaussian model computed using PosteriorStacker. Mean and standard deviation of each curve are: $\mu = 2.10$, $\sigma = 0.27$ (Population A, yellow) and $\mu = 1.86$, $\sigma = 0.16$ (Population B, green) with error bands corresponding to the 1-sigma interval.

The results can also be obtained for the different sub-types, as shown in Figure 26. An interesting feature to note is that the probability distributions seem to go from lower mean values of the photon index with higher probability towards higher mean Γ values and wider distributions as they change from types B to types A and xA. The difference between the

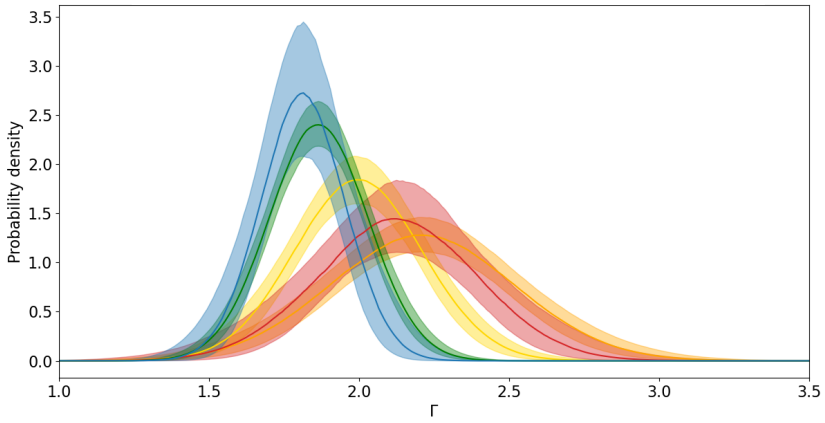

Figure 26: Sample probability distributions for the photon index (Γ)of the best fit following the Gaussian model computed using PosteriorStacker. The population subtypes presented are B+ (blue), B (green), A1 (yellow), A2 (orange) and xA (red) with error bands corresponding to the 1-sigma interval. Mean and standard deviation of each curve are: $\mu = 1.81$ and $\sigma = 0.15$ (B+); $\mu = 1.86$, $\sigma = 0.17$ (B); $\mu = 2.00$, $\sigma = 0.22$ (A1); $\mu = 2.21$, $\sigma = 0.31$ (A2) and $\mu = 2.13$, $\sigma = 0.28$ (xA).

sub-types is also more apparent in this case than in Figure 23 where the hard photon index results were presented.

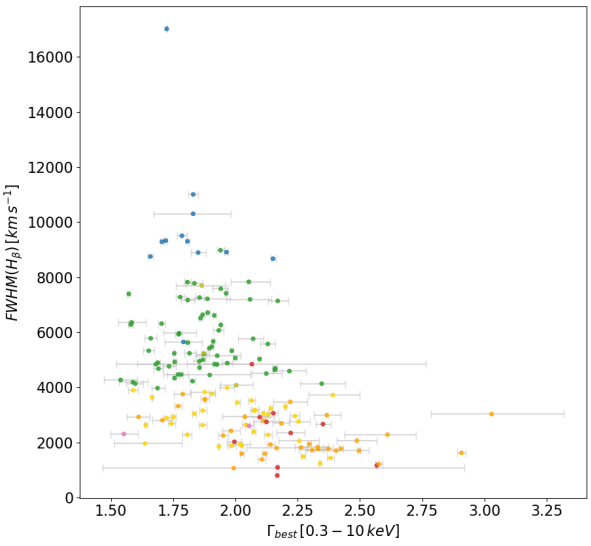

Figure 27: FWHM(Hβ) against the photon index from the best fit model for each source ($\Gamma_{abs}[0.3-10keV]$) with error bars corresponding to the 16% and 84% quantiles. The spectral sub-types of the 160 sources are presented here as: A1 (yellow), A2 (orange), A3 (red), A4 (pink), B1 (green), B1+ (blue) and B2 (olive).

It is also of interest to relate the final resulting gamma value of the best fit for each source to the optical parameters of the quasar main sequence. In Figure 27 FWHM($H\beta$) is plotted

against the final photon index for the 160 sources, color coded by their sub-type. As it was already observed in Figure 24 for the simple power-law model, objects tend to have a higher photon index as their FWHM($H\beta$) decreases, although some of the sources with higher Γ or high acretors (types A2 and A3) have larger error bars. In this case, the three sources with larger errors have a lower number of counts (less than 700 in the 0.3-10 keV energy range) that result in parameters with larger uncertainties.

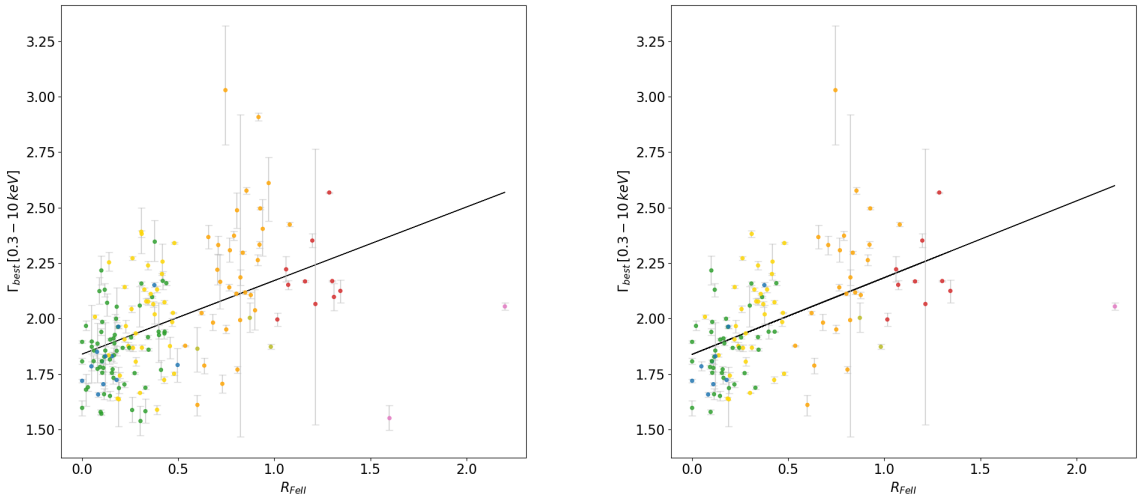

(a) (b)

Figure 28: Photon index from the best fit model for each source ($\Gamma_{best}[0.3-10keV]$) against R_{FeII} with error bars corresponding to the 16% and 84% quantiles. The spectral sub-types of the 160 sources are presented here as: A1 (yellow), A2 (orange), A3 (red), A4 (pink), B1 (green), B1+ (blue) and B2 (olive). Point with an arrow is a upper limit for an object with $R_{FeII} < 0.05$. Left: the linear regression of the data (with 95% confidence interval): $\Gamma_{best} = (0.3 \pm 0.1)R_{FeII} + (1.84 \pm 0.06)$, Pearson correlation coefficient $r = 0.48$ and p-value $p = 1.65 \cdot 10^{-10}$. Right: linear regression of the data removing sources with z>0.4: $\Gamma_{best} = (0.3 \pm 0.1)R_{FeII} + (1.84 \pm 0.05)$, Pearson correlation coefficient $r = 0.54$ and p-value $p = 3.9 \cdot 10^{-10}$.

The other parameter is R_{FeII} related to the accretion rate of the quasar. The photon index of the best fit is plotted against R_{FeII} in Figure 28a for the 160 sources. Observing the plot, there is a tendency for the photon index to increase as R_{FeII} increases, so a linear regression is carried out to find a possible correlation. The result is a line with equation $\Gamma_{best} = 0.3R_{FeII} + 1.84$ and a Pearson correlation coefficient $r = 0.48$. Some outliers like the two sources of type A4 with a flatter photon index could affect this result. It is also important to take into account the effects of redshift, as the soft excess is no longer visible for objects at $z > 0.4$. In Figure 28b the remaining 118 sources with redshift $z < 0.4$ are plotted, with a linear regression with a higher correlation coefficient $r = 0.54$. Although the correlation coefficients are not very significant, the tendency is clear and stronger when we only consider objects with redshifts that still permit the black-body to be visible. This is yet another evidence of a relation between the X-ray photon index and the accretion rate of quasars.

With respect of the luminosity (results for the best-fit $log_{10}L_{pl}$ in Figure 20) it is also interesting to study its relation to other properties of AGN measured through their optical spectra. The data of bolometric luminosity ($log_{10}L_{bol}(5100\text{Å})$), the mass of the black hole (M_{BH}) and the Eddington ratio ($\lambda_{Edd} = L_{bol}/L_{Edd}$), for the ZMS sources have been computed. We are able to make a comparison between these properties and the results obtained for the X-ray luminosity.

Separating the sample into the two populations, we find that there is no significant difference between the luminosities of Population A and B, with medians Med(A)= 45.58 and Med(B)=46.04. There is a bigger difference in the case of M_{BH}, where we obtained for each population the median values of $log_{10}M_{BH}$: Med(A)=7.92 and Med(B)=8.95. Finally, for the Eddington ratio, the two populations present very distinct distributions. The median λ_{Edd} for Population A is Med(A)=0.41 while for Population B the value is Med(B)=0.07.

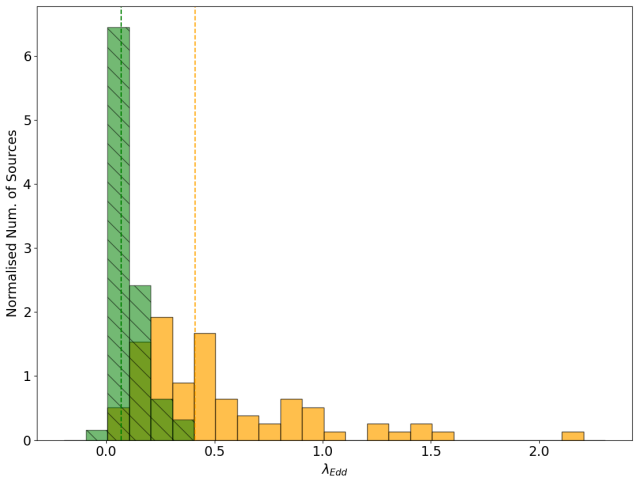

Figure 29: Eddington ratio for the objects of the ZMS sample with a best fit. Sources of Population A are displayed in yellow and Population B in green with the dashed lines representing their median values: $Med(A) = 0.41$ and $Med(B) = 0.07$.

The wide spread in the distribution of Population A is an interesting feature that it is also observed for the photon index probability distributions of this population in Figures 25 and 26.

This seems to indicate that the differences in X-ray luminosity between the two quasar populations is more related to the Eddington ratio (and/or the mass of the black hole). The latter are properties closely related to the R_{FeII} parameter of the main sequence and the accretion properties of the source: a high λ_{Edd} is expected in extreme accretors from Population A while lower values belong to Population B quasars with a more massive black hole.

4.3 Soft-excess

As one of the aims of this work is to study the importance of the X-ray soft excess and especially its role in quasars of Population A (high accretors), we have to try to quantify it by using the black-body component.

In Figure 30 a spectrum with a clear soft excess is shown as an example of a source that needs the black-body component. In the second plot, showing the residuals, there is a clear excess of emission with respect to the power-law model to which it has been fitted (red and orange lines).

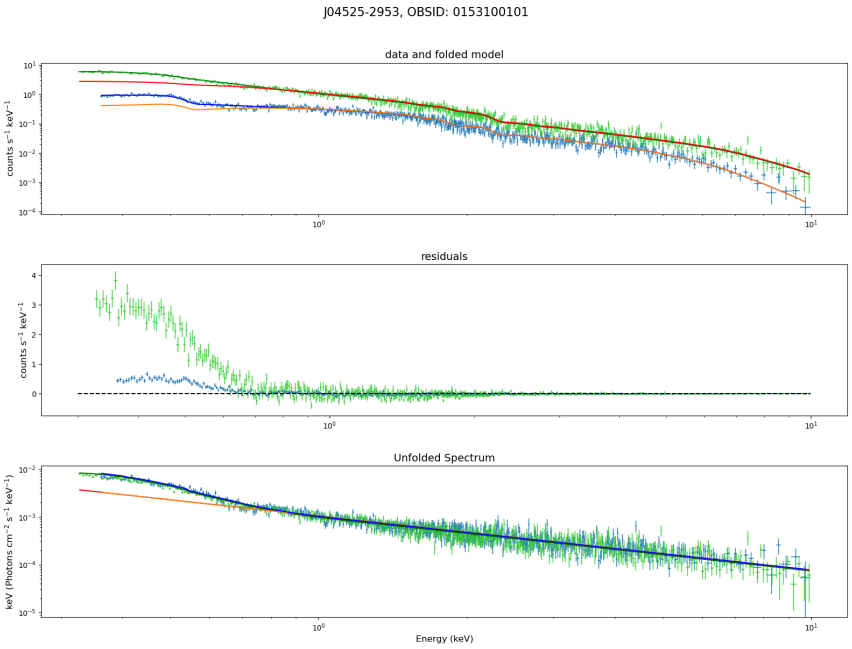

Figure 30: Example of a BXA plot showing the fit to the absorbed model with black-body (green and blue lines) and the simple power-law model (red and orange lines).

In order to measure the strength of the black-body and its importance for the different populations, its luminosity and that of the power-law are used. The luminosity of the black-body used to model the soft excess is calculated in the 0.5-2 keV energy band, so we must first compute the luminosity of the power-law in that same range. For that, an extrapolation is made using PyXspec. This is done for all 160 sources, including those that do not present a very significant soft excess, in order to measure its significance of the black-body for all the sub-types. The ratio of the two values of luminosity, L_{bb}/L_{pl} is presented in Figure 31a.

The distributions are similar between $L_{bb}/L_{pl} = 10^{-1}$ and $L_{bb}/L_{pl} = 1$ although type A objects present a higher ratio in favor of the black-body luminosity with a median for the distribution of $L_{bb}/L_{pl} = 0.26$ while the value for Population B is $L_{bb}/L_{pl} = 0.21$. Nevertheless, there are noticeable differences in the outliers, as the majority of sources with a ratio below $L_{bb}/L_{pl} = 10^{-2}$ are of type B while the only objects with a ratio

$L_{bb}/L_{pl} > 1$ are of type A.

The results seem to point to a black-body component more significant in Population A sources, although a difference between the distributions cannot be stated with great confidence as the K-S test p-value is $p = 0.02$.

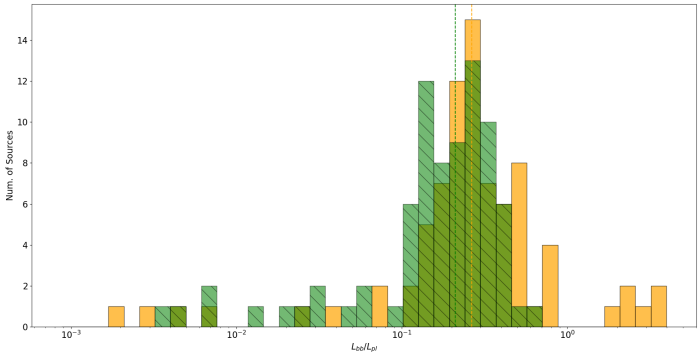

(a)

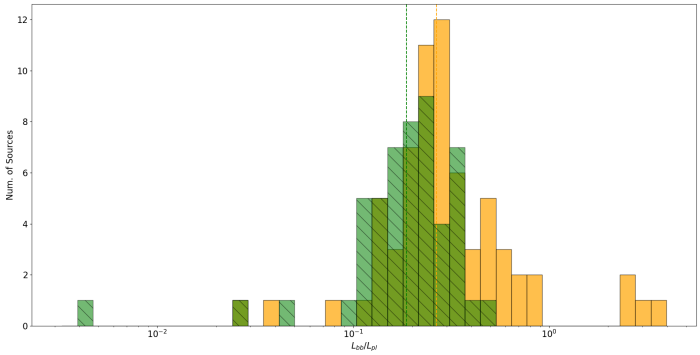

(b)

Figure 31: Ratio between the black-body and the power-law luminosity in the [0.5-2 keV] band L_{bb}/L_{pl}. Sources of Population A are displayed in yellow and Population B in green with the dashed lines representing their median values. (a) Ratio for the 160 sources, with $Med(A) = 0.26$, $Med(B) = 0.21$. K-S test p-value $p = 0.02$. (b) Ratio for the 118 sources with z<0.4 $Med(A) = 0.27$, $Med(B) = 0.19$. K-S test p-value $p = 0.0052$.

Most sources with $L_{bb}/L_{pl} > 1$ are type A3. The ones with $L_{bb}/L_{pl} < 10^{-2}$ all have redshift z>0.4. In these cases, although still statistically significant, the black body component cannot be properly constrained, as it gradually moves outside the energy range under consideration as redshift increases. Once sources with z>0.4 are removed (leaving 118 objects, see Figure 31b), the K-S test p-value becomes $p = 0.0052$ and the only source remaining with $L_{bb}/L_{pl} < 10^{-2}$ is of Population B.

5 Conclusions

In this work we aimed to study the X-ray spectral properties of quasars in relation to their classification in the main sequence, in order to describe how X-ray parameters such as the

photon index are linked to the optical parameters (FWHM(Hβ) and R_{FeII}) that define the two populations of quasars. Of special interest is the analysis of the X-ray soft excess that has been observed mainly in Population A, i.e. high accreting quasars.

To this end, we have compiled a sample of optically selected quasars and found their counterparts in the 4XMM-DR12 catalogue where spectral data is available. We have studied a final sample of 207 sources that comprises quasars of both populations (103 and 104 respectively for Population A and B) and their sub-types.

We performed a comprehensive spectral X-ray analysis for all 207 sources using Bayesian statistics and fitting their spectra to four different models: a power-law limited to the hard X-rays band; then, considering the whole range from 0.3 to 10 keV, an absorbed power-law; an absorbed power-law with a black-body component to quantify the soft excess and a double power-law. By using the tool BXA (Bayesian X-ray Analysis), from each fit we are able to study the posterior distribution of the parameters.

The main conclusions that can be extracted from the results presented in this work are:

- We observe significant differences between the results of the hard photon index for each population, with objects of Population A showing a steeper profile for their power-law than those of Population B. This establishes a relation between the hard X-ray photon index and the accretion rate of quasars with higher values of Γ_{hard} corresponding to the high accreting sources (Population A of the quasar main sequence). When comparing the values of Γ_{hard} to the photon index of the absorbed power-law (0.3-10 keV), we also observe that Population A sources (especially A2 and A3; see Fig. 14) present bigger differences as a result of the soft X-ray excess.

- The spectra of 160 sources can be described either with an absorbed power-law or by adding a black-body component to this model. The results of the best-fit photon index for these objects indicate that the differences between populations A and B found in the hard X-ray band become more significant when considering the soft emission. This is further evidence for the presence of a soft excess in objects of Population A that lead to a higher photon index. The Gaussian probability distributions for this parameter also show that there is a distinction between the spectral sub-types, from B+ quasars (low accretion rate, larger M_{BH} and high values of FWHM(H_β)) that present lower values of Γ to quasars of type xA (extreme accretors with smaller M_{BH}) with a higher photon index.

- For 47 sources the double power-law constitutes an acceptable fit for 17 of them, which need a different analysis that does not relate to the soft excess. The remaining 30 sources could not be fitted to any of the four models due to the complexity of their spectra, and 6 of them were identified as well-known variable quasars with previous studies.

- The results for the computed ratio of black-body and power-law luminosity, L_{bb}/L_{pl}, indicate as well that the soft excess is more significant for extreme accretors. The majority of sources with $L_{bb}/L_{pl} > 1$ are of type A2 or A3, while the lowest values

correspond mainly to Population B quasars. All Population A quasars with $L_{bb}/L_{pl} < 10^{-2}$ have redshift $z > 0.4$, which means that the soft excess is lost from the spectrum, explaining the low values for objects of type A. After removing the sources with $z > 0.4$ we find a more significant difference between both populations. All the results of this work point to a relation between the X-ray photon index and the accretion rate of the quasar, and are consistent with observations of the X-ray soft emission present mainly in sources of Population A.

5.1 Future work

In this work we have found significant differences between Population A and B of quasars based on a sample of 207 sources. A more in-depth and individual analysis that was out of the scope of this work could be done as well to find an acceptable model for sources with a more complex spectrum. The quasar main sequence is also related to other measured properties of the sources, like the mass of the central black hole or their Eddington ratio, that could present a correlation to X-ray parameters like the photon index and remain to be studied.

Expanding the size of the sample in future studies would increase the reliability of the results. Especially for extreme accretors (sources of types A3, A4), since they are the less numerous while being essential for the understanding of the X-ray soft excess observed at ∼0.3-10 KeV. A larger sample would also help us find stronger evidence of some of the trends observed in this work, like the relation between the best-fit photon index and the intensity ratio of the $FeII$ blend, R_{FeII}; or the increasing dispersion of the Gaussian distributions for Γ as we go from low accretion objects (B+) towards the extreme accretors (xA).

The Sloan Digital Sky Survey (SDSS) offers a large sample of sources that could be studied as a continuation of this work. A crossmatch between the SDSS DR16 (Lyke et al., 2020) and the 4XMM-DR12 catalogue has already been made, resulting in a list of more than 12000 quasars with available X-ray spectral data.

References

K. Arnaud, C. Gordon, B. Dorman, and K Rutkowski. Xspec. an x-ray spectral fitting package. users' guide for version 12.13. https://heasarc.gsfc.nasa.gov/xanadu/xspec/manual/XspecManual.html.

K. A. Arnaud. XSPEC: The First Ten Years. In George H. Jacoby and Jeannette Barnes, editors, Astronomical Data Analysis Software and Systems V, volume 101 of Astronomical Society of the Pacific Conference Series, page 17, January 1996.

L Baronchelli, K Nandra, and J Buchner. Relativistic accretion disc reflection in AGN x-ray spectra aat z=0.5-4: a study of four chandra deep fields. MNRAS, 498(4):5284–5298, 2020. doi: 10.1093/mnras/staa2684.

V. Beckman and C. Shrader. Active Galactic Nuclei. WILEY-VCH Verlag, 2012.

HI4PI Collaboration: N. Ben Bekhti, L. Flöer, R. Keller, J. Kerp, D. Lenz, B. Winkel, J. Bailin, M. R. Calabretta, L. Dedes, H. A. Ford, B. K. Gibson, U. Haud, S. Janowiecki, P. M. W. Kalberla, F. J. Lockman, N. M. McClure-Griffiths, T. Murphy, H. Nakanishi, D. J. Pisano, and L. Staveley-Smith. HI4PI: a full-sky hi survey based on EBHIS and GASS. A&A, 594:A116, 2016. doi: 10.1051/0004-6361/201629178.

Rozenn Boissay, Claudio Ricci, and Stéphane Paltani. A hard x-ray view of the soft excess in AGN. A&A, 588:A70, 2016. doi: 10.1051/0004-6361/201526982.

Todd A. Boroson and Richard F. Green. The emission-line properties of low-redshift quasi-stellar objects. ApJS, 80:109, 1992. doi: 10.1086/191661.

J. Buchner, A. Georgakakis, K. Nandra, L. Hsu, C. Rangel, M. Brightman, A. Merloni, M. Salvato, J. Donley, and D. Kocevski. X-ray spectral modelling of the AGN obscuring region in the CDFS: Bayesian model selection and catalogue. A&A, 564:A125, 2014. doi: 10.1051/0004-6361/201322971.

Johannes Buchner. Ultranest – a robust, general purpose bayesian inference engine, 2021.

M. Cappi, B. De Marco, G. Ponti, F. Ursini, P.-O. Petrucci, S. Bianchi, J. S. Kaastra, G. A. Kriss, M. Mehdipour, M. Whewell, N. Arav, E. Behar, R. Boissay, G. Branduardi-Raymont, E. Costantini, J. Ebrero, L. Di Gesu, F. A. Harrison, S. Kaspi, G. Matt, S. Paltani, B. M. Peterson, K. C. Steenbrugge, and D. J. Walton. Anatomy of the AGN in NGC 5548. A&A, 592:A27, 2016. doi: 10.1051/0004-6361/201628464.

W. Cash. Parameter estimation in astronomy through application of the likelihood ratio. ApJ, 228:939–947, March 1979. doi: 10.1086/156922.

V. Ganci, P. Marziani, M. D'Onofrio, A. del Olmo, E. Bon, N. Bon, and C. A. Negrete. Radio loudness along the quasar main sequence. A&A, 630:A110, 2019. doi: 10.1051/0004-6361/201936270.

M. Gliozzi, I. E. Papadakis, M. Eracleous, R. M. Sambruna, D. R. Ballantyne, V. Braito, and J. N. Reeves. Short-term variability and PSD analysis of the radio-loud AGN 3C 390.3, 2009.

Craig Gordon and Keith Arnaud. PyXspec: Python interface to XSPEC spectral-fitting program. Astrophysics Source Code Library, record ascl:2101.014, January 2021.

Jesse L. Greenstein and Maarten Schmidt. The Quasi-Stellar Radio Sources 3C 48 and 3C 273. ApJ, 140:1, July 1964. doi: 10.1086/147889.

Harold Jeffreys. Theory of probability-international series of monographs on physics, 1961.

K. I. Kellermann, J. J. Condon, A. E. Kimball, R. A. Perley, and Željko Ivezić. Radio-loud and Radio-quiet QSOs. ApJ, 831(2):168, November 2016. doi: 10.3847/0004-637X/831/2/168.

N. Kumari, M. Pal, S. Naik, A. Jana, G. K. Jaisawal, and P. Kushwaha. Complex optical/UV and x-ray variability in seyfert 1 galaxy mrk 509. Publications of the Astronomical Society of Australia, 38, 2021. doi: 10.1017/pasa.2021.41.

Brad W. Lyke, Alexandra N. Higley, J. N. McLane, Danielle P. Schurhammer, Adam D. Myers, Ashley J. Ross, Kyle Dawson, Solène Chabanier, Paul Martini, Nicolás G. Busca, Hélion du Mas des Bourboux, Mara Salvato, Alina Streblyanska, Pauline Zarrouk, Etienne Burtin, Scott F. Anderson, Julian Bautista, Dmitry Bizyaev, W. N. Brandt, Jonathan Brinkmann, Joel R. Brownstein, Johan Comparat, Paul Green, Axel de la Macorra, Andrea Muñoz Gutiérrez, Jiamin Hou, Jeffrey A. Newman, Nathalie Palanque-Delabrouille, Isabelle Pâris, Will J. Percival, Patrick Petitjean, James Rich, Graziano Rossi, Donald P. Schneider, Alexander Smith, M. Vivek, and Benjamin Alan Weaver. The Sloan Digital Sky Survey Quasar Catalog: Sixteenth Data Release. ApJS, 250(1):8, September 2020. doi: 10.3847/1538-4365/aba623.

P. Marziani, J. W. Sulentic, D. Dultzin-Hacyan, M. Calvani, and M. Moles. Comparative Analysis of the High- and Low-Ionization Lines in the Broad-Line Region of Active Galactic Nuclei. ApJS, 104:37, May 1996. doi: 10.1086/192291.

P. Marziani, J. W. Sulentic, T. Zwitter, D. Dultzin-Hacyan, and M. Calvani. Searching for the Physical Drivers of the Eigenvector 1 Correlation Space. ApJ, 558(2):553–560, September 2001. doi: 10.1086/322286.

P. Marziani, J. W. Sulentic, R. Zamanov, M. Calvani, D. Dultzin-Hacyan, R. Bachev, and T. Zwitter. An optical spectroscopic atlas of low-redshift active galactic nuclei. ApJS, 145(2):199, 2003. doi: 10.1086/346025.

P. Marziani, M. DOnofrio, A. del Olmo, and D. Dultzin. Quasars at all Cosmic Epochs. September 2018a. doi: 10.3389/978-2-88945-604-8.

Paola Marziani, Deborah Dultzin, Jack W. Sulentic, Ascensión Del Olmo, C. A. Negrete, Mary L. Martínez-Aldama, Mauro D'Onofrio, Edi Bon, Natasa Bon, and Giovanna M. Stirpe. A main sequence for quasars. Frontiers in Astronomy and Space Sciences, 5:6, March 2018b. doi: 10.3389/fspas.2018.00006.

Marziani, P., del Olmo, A., Martínez-Carballo, M. A., Martínez-Aldama, M. L., Stirpe, G. M., Negrete, C. A., Dultzin, D., D´Onofrio, M., Bon, E., and Bon, N. Black hole mass estimates in quasars - a comparative analysis of high- and low-ionization lines. A&A, 627:A88, 2019. doi: 10.1051/0004-6361/201935265.

M. Mehdipour, G. Branduardi-Raymont, and M. J. Page. The warm absorber and x-ray variability of the seyfert 1 galaxy NGC 3516 as seen by the XMM-Newton RGS. A&A, 514:A100, 2010. doi: 10.1051/0004-6361/200913049.

NASA/GSFC. NASA's HEASARC. high energy astrophysics science archive research center. https://heasarc.gsfc.nasa.gov/.

J. Newman, S. Tsuruta, A. C. Liebmann, H. Kunieda, and Y. Haba. Combined analysis of x-ray spectra of NGC 3227. ApJ, 907(1):45, 2021. doi: 10.3847/1538-4357/abd1da.

P. Padovani, D. M. Alexander, R. J. Assef, B. De Marco, P. Giommi, R. C. Hickox, G. T. Richards, V. Smolčić, E. Hatziminaoglou, V. Mainieri, and M. Salvato. Active galactic nuclei: what's in a name? The Astronomy and Astrophysics Review, 25(1), 2017. doi: 10.1007/s00159-017-0102-9.

S. Panda and P. Marziani. High eddington quasars as discovery tools: current state and challenges. Frontiers in Astronomy and Space Sciences, 10, 2023. doi: 10.3389/fspas.2023.1130103.

P.O. Petrucci, F. Ursini, A. De Rosa, S. Bianchi, M. Cappi, G. Matt, M. Dadina, and J. Malzac. Testing warm comptonization models for the origin of the soft x-ray excess in AGNs. A&A, 611:A59, 2018.

L.C. Popovic, A.I. Shapovalova, D. Ilic, A. Kovacevic, W. Kollatschny, A.N. Burenkov, V.H. Chavushyan, N.G. Bochkarev, and J. Leon-Tavares. Spectral optical monitoring of 3c 390.3 in 1995–2007. A&A, 528:A130, 2011. doi: 10.1051/0004-6361/201016317.

R. Serafinelli, V. Braito, P. Severgnini, F. Tombesi, G. Giani, E. Piconcelli, R. Della Ceca, F. Vagnetti, M. Gaspari, F. G. Saturni, R. Middei, and A. Tortosa. X-ray obscuration from a variable ionized absorber in PG 1114+445. A&A, 654:A32, 2021. doi: 10.1051/0004-6361/202141474.

Carl K. Seyfert. Nuclear Emission in Spiral Nebulae. ApJ, 97:28, January 1943. doi: 10.1086/144488.

Yue Shen and Luis C. Ho. The diversity of quasars unified by accretion and orientation. Nature, 513(7517):210–213, September 2014. doi: 10.1038/nature13712.

K.P. Singh, G.P. Garmire, and J. Nousek. Observations of Soft X-Ray Spectra from a Seyfert 1 and a Narrow Emission-Line Galaxy. ApJ, 297:633, 1985. doi: 10.1086/163560.

J. W. Sulentic, P. Marziani, and D. Dultzin-Hacyan. Phenomenology of broad emission lines in active galactic nuclei. ARA&A, 38:521–571, January 2000a. doi: 10.1146/annurev.astro.38.1.521.

J. W. Sulentic, T. Zwitter, P. Marziani, and D. Dultzin-Hacyan. Eigenvector 1: An Optimal Correlation Space for Active Galactic Nuclei. ApJL, 536(1):L5–L9, June 2000b. doi: 10.1086/312717.

J. W. Sulentic, S. Zamfir, P. Marziani, and D. Dultzin. Our Search for an H-R Diagram of Quasars. In Revista Mexicana de Astronomia y Astrofisica Conference Series, volume 32, pages 51–58, April 2008. doi: 10.48550/arXiv.0709.2499.

Jack W. Sulentic, Rumen Bachev, Paola Marziani, C. Alenka Negrete, and Deborah Dultzin. C IV λ1549 as an eigenvector 1 parameter for active galactic nuclei. ApJ, 666(2):757–777, 2007. doi: 10.1086/519916.

M. B. Taylor. TOPCAT & STIL: Starlink Table/VOTable Processing Software. In P. Shopbell, M. Britton, and R. Ebert, editors, Astronomical Data Analysis Software and Systems XIV, volume 347 of Astronomical Society of the Pacific Conference Series, page 29, December 2005.

Matthew J. Temple, James H. Matthews, Paul C. Hewett, Amy L. Rankine, Gordon T. Richards, Manda Banerji, Gary J. Ferland, Christian Knigge, and Matthew Stepney. Testing AGN outflow and accretion models with C IV and He II emission line demographics in z $\approx$ 2 quasars. MNRAS, 523(1):646–666, July 2023. doi: 10.1093/mnras/stad1448.

Prakash Tripathi and Gulab Chand Dewangan. Thermal comptonization in a changing corona in the changing-look active galaxy NGC 1566. ApJ, 930(2):117, 2022. doi: 10.3847/1538-4357/ac610f.

C. Megan Urry and Paolo Padovani. Unified schemes for radio-loud active galactic nuclei. Publications of the Astronomical Society of the Pacific, 107:803, 1995. doi: 10.1086/133630.

Y. Wang, J. Kaastra, M. Mehdipour, J. Mao, E. Costantini, G. A. Kriss, C. Pinto, G. Ponti, E. Behar, S. Bianchi, G. Branduardi-Raymont, B. De Marco, S. Grafton-Waters, P. Petrucci, J. Ebrero, D. James Walton, S. Kaspi, Y. Xue, S. Paltani, L. di Gesu, and Z. He. Transient obscuration event captured in NGC 3227. A&A, 657:A77, 2022. doi: 10.1051/0004-6361/202141599.

N. A. Webb, M. Coriat, I. Traulsen, J. Ballet, C. Motch, F. J. Carrera, F. Koliopanos, J. Authier, I. de la Calle, M. T. Ceballos, E. Colomo, D. Chuard, M. Freyberg, T. Garcia, M. Kolehmainen, G. Lamer, D. Lin, P. Maggi, L. Michel, C. G. Page, M. J. Page, J. V. Perea-Calderon, F.-X. Pineau, P. Rodriguez, S. R. Rosen, M. Santos Lleo, R. D.

Saxton, A. Schwope, L. Tomá s, M. G. Watson, and A. Zakardjian. The xmm-newton serendipitous survey. A&A, 641:A136, 2020. doi: 10.1051/0004-6361/201937353.

Lisa M. Winter, Richard F. Mushotzky, Jack Tueller, and Craig Markwardt. X-ray properties of an unbiased hard x-ray–detected sample of active galactic nuclei. ApJ, 674(2): 686–710, 2008. doi: 10.1086/525274.

Julien Wolf, Mara Salvato, Damien Coffey, Andrea Merloni, Johannes Buchner, Riccardo Arcodia, Dalya Baron, Francisco J. Carrera, Johan Comparat, Donald P. Schneider, and Kirpal Nandra. Exploring the diversity of Type 1 active galactic nuclei identified in SDSS-IV/SPIDERS. MNRAS, 492(3):3580–3601, March 2020. doi: 10.1093/mnras/staa018.

XMM-Newton. XMM-Newton: A technical description. Webpage.

Zhibo Yu, Jiachen Jiang, Cosimo Bambi, Luigi C Gallo, Dirk Grupe, Andrew C Fabian, Christopher S Reynolds, and William N Brandt. An XMM-newton study of six narrow-line seyfert 1 galaxies at z=0.35-0.92. MNRAS, 522:5456–5468, 2023. doi: 10.1093/mnras/stad1327.

S. Zamfir, J. W. Sulentic, P. Marziani, and D. Dultzin. Detailed characterization of hβ emission line profile in low-z SDSS quasars. MNRAS, 403(4):1759–1786, 2010. doi: 10.1111/j.1365-2966.2009.16236.x.

A Summary table of the 207 studied sources

In the following tables, all the sources studied in this work along with their name, coordinates, redshift, spectral type, the number of observations made by XMM-Newton and the model for the best fit are presented.

Nombre	RA	DEC	z	Spectral Type 4DE1	Num. of obs.	Best fit model
J020514.77-045639.7	2 05 14.8	-4 56 39.7	0.3618	B1	2	absorbed pl
J020809.63-053839.1	2 08 09.6	-5 38 39.1	0.6422	B1	2	absorbed pl with bb
J021640.73-044404.8	2 16 40.7	-4 44 04.8	0.875	B1	2	absorbed pl with bb
J021705.52-042253.5	2 17 05.5	-4 22 54.7	0.7884	B1	1	absorbed pl
J023322.16-045506.8	2 33 22.2	-4 55 06.9	0.7804	B1	2	absorbed pl with bb
J091011.14+542723.5	9 10 11.1	54 27 23.7	0.622	B1	1	absorbed pl with bb
J093301.58+495029.9	9 33 01.6	49 50 27.8	0.6158	B1	1	absorbed pl
J102152.49+131146.4	10 21 52.5	13 11 46.3	0.55	B2	1	absorbed pl with bb
J110505.47+251527.3	11 05 05.5	25 15 27.1	0.4125	B1	1	absorbed pl
J112946.01-012140.5	11 29 46.0	-1 21 40.5	0.7264	B1	1	absorbed pl with bb
J120734.62+150643.7	12 07 34.6	15 06 43.7	0.7507	A2	1	absorbed pl with bb
J125701.71+281230.0	12 57 01.7	28 12 30.1	0.3059	B1+	2	double pl
J125752.74+475020.6	12 57 52.8	47 50 21.1	0.5282	A1	3	absorbed pl
J131933.02+550808.5	13 19 33.0	55 08 08.7	0.3283	B1	1	absorbed pl with bb
J134751.58+283629.7	13 47 51.6	28 36 29.7	0.7406	B1	1	absorbed pl with bb
J140626.60+250921.0	14 06 26.6	25 09 21.0	0.8668	B1	1	absorbed pl with bb
J140843.78+540751.4	14 08 43.8	54 07 51.4	0.9182	B1	1	absorbed pl
J142129.75+474724.5	14 21 29.8	47 47 24.0	0.0726	B1	1	absorbed pl with bb
J161603.77+463225.2	16 16 03.8	46 32 25.2	0.95	B1	1	absorbed pl with bb
J172109.49+354216.0	17 21 09.5	35 42 15.8	0.2833	B1	1	absorbed pl
J212939.40-000719.7	21 29 39.4	-0 07 19.5	0.5534	B1++	2	double pl

Table 6: The 21 sources from Ganci et al. (2019) used in this work. "Best fit model" column presents the preferred model for each source: absorbed power-law, absorbed power-law with black-body or double power-law.

Name	RA	DEC	z	Spectral Type 4DE1	Num. of obs.	Best fit model
J00059+1609	0 05 59.3	16 09 49.8	0.4504	B1	1	absorbed pl with bb
J00063+2012	0 06 19.5	20 12 10.7	0.0252	A1	7	absorbed pl with bb
J00105+1058	0 10 31.0	10 58 29.4	0.09	B1	2	absorbed pl with bb
J00292+1316	0 29 13.7	13 16 04.0	0.142	A1	1	absorbed pl with bb
J00457+0410	0 45 47.2	4 10 23.4	0.385	B2	1	double pl
J00519+1725	0 51 54.5	17 25 58.0	0.064	B1	1	absorbed pl with bb
J00535+1241	0 53 34.9	12 41 36.0	0.061	A3	5	absorbed pl with bb
J00548+2525	0 54 52.2	25 25 39.3	0.155	B1	2	absorbed pl with bb
J00573-2222	0 57 20.2	-22 22 56.4	0.062	A2	4	-
J00586-3606	0 58 37.4	-36 06 04.1	0.162	B1	3	absorbed pl with bb
J01237-5848	1 23 45.7	-58 48 20.5	0.0461	B1	4	absorbed pl with bb
J01342-4258	1 34 16.9	-42 58 26.0	0.237	A4	2	absorbed pl with bb
J02078+0242	2 07 49.9	2 42 55.5	0.155	A1	1	absorbed pl with bb
J02145-0046	2 14 33.6	-0 46 00.0	0.027	A1	2	absorbed pl with bb

Name	RA	DEC	z	Spectral Type 4DE1	Num. of obs.	Best fit model
J02346-0847	2 34 37.8	-8 47 16.1	0.043	B1	5	-
J02449+6228	2 44 57.7	62 28 06.1	0.045	B2++	1	double pl
J04078-1211	4 07 48.4	-12 11 36.7	0.574	B1	2	absorbed pl with bb
J04200-5456	4 20 00.4	-54 56 16.5	0.0051	B1	5	-
J04331+0521	4 33 11.1	5 21 16.3	0.033	A1	4	-
J04363-1022	4 36 22.3	-10 22 33.9	0.035	A1	1	absorbed pl with bb
J04525-2953	4 52 30.2	-29 53 35.2	0.2855	A1	1	absorbed pl with bb
J05161-0009	5 16 11.4	-0 08 59.2	0.033	B2	6	-
J07086-4933	7 08 41.5	-49 33 06.7	0.0408	A3	11	-
J07580+3920	7 58 00.1	39 20 29.0	0.096	A1	2	-
J08045+6459	8 04 30.5	64 59 52.1	0.148	A3	1	absorbed pl with bb
J08109+7602	8 10 58.8	76 02 42.2	0.1	A1	3	absorbed pl with bb
J08407+1312	8 40 47.6	13 12 24.2	0.6804	A2	1	absorbed pl with bb
J08447+7653	8 44 45.3	76 53 09.4	0.131	A2	1	absorbed pl with bb
J08477+3445	8 47 42.4	34 45 04.4	0.064	A2	2	absorbed pl with bb
J09065+1646	9 06 31.9	16 46 11.8	0.4113	B1	1	absorbed pl with bb
J09184+1618	9 18 26.0	16 18 19.7	0.029	B1	2	-
J09259+1954	9 25 54.7	19 54 05.0	0.19	B1	1	double pl
J09260+1244	9 26 03.3	12 44 03.7	0.028	A1	1	absorbed pl with bb
J09568+4115	9 56 52.4	41 15 22.3	0.2347	A1	2	absorbed pl with bb
J10040+2855	10 04 02.6	28 55 35.0	0.329	A2	3	absorbed pl with bb
J10143-0418	10 14 20.7	-4 18 40.1	0.058	A1	1	absorbed pl with bb
J10235+1951*	10 23 30.5	19 51 54.4	0.0039	B1	6*	-
J10319-1416	10 31 54.3	-14 16 51.5	0.086	B1	2	absorbed pl with bb
J10514-0918	10 51 29.9	-9 18 10.3	0.345	B1+	1	absorbed pl with bb
J11042+7658	11 04 13.9	76 58 58.2	0.3116	B1	1	absorbed pl with bb
J11065-0052	11 06 31.8	-0 52 52.3	0.426	B1	1	absorbed pl with bb
J11067+7234*	11 06 47.3	72 34 07.4	0.0088	B1	6*	-
J11191+2119	11 19 08.7	21 19 17.9	0.177	A1	5	absorbed pl with bb
J11292-0424	11 29 16.7	-4 24 07.4	0.06	A2	8	-
J11311+3114	11 31 09.5	31 14 05.5	0.289	B1	2	absorbed pl with bb
J11364+2135	11 36 29.4	21 35 45.7	0.03	A2	1	absorbed pl with bb
J11390-3744	11 39 01.8	-37 44 19.5	0.009	A1	1	-
J11456-1827	11 45 40.5	-18 27 15.0	0.033	A2	5	absorbed pl with bb
J11520-1122	11 52 03.4	-11 22 22.8	0.049	A1	1	absorbed pl with bb
J12047+2754	12 04 42.1	27 54 12.2	0.1654	B1	2	absorbed pl with bb
J12142+1403	12 14 17.7	14 03 13.2	0.0811	A1	10	absorbed pl with bb
J12184+2948	12 18 26.5	29 48 46.1	0.0124	A3	6	-
J12193+0638	12 19 20.9	6 38 38.5	0.3322	B1	2	absorbed pl with bb
J12217+7518	12 21 44.1	75 18 38.7	0.0711	A1	4	-
J12291+0203	12 29 06.7	2 03 07.9	0.158	A1	14	absorbed pl with bb
J12320+2009	12 32 03.6	20 09 29.5	0.064	A1	1	absorbed pl with bb
J12396-0520	12 39 39.4	-5 20 39.8	0.009	B2	6	-
J13055-1033	13 05 33.0	-10 33 19.5	0.2783	A2	1	absorbed pl with bb
J13097+0819	13 09 47.0	8 19 48.2	0.1546	B1	2	absorbed pl with bb
J13122+3515	13 12 17.8	35 15 21.0	0.1821	B1	1	absorbed pl with bb
J13130-1107	13 13 05.9	-11 07 42.6	0.034	A1	1	absorbed pl with bb
J13238+6541	13 23 49.5	65 41 48.2	0.168	A1	2	absorbed pl with bb
J13253-3824	13 25 19.4	-38 24 52.1	0.0667	A1	15	absorbed pl with bb
J13360+1725	13 36 02.0	17 25 13.1	0.554	A1	1	absorbed pl with bb

Name	RA	DEC	z	Spectral Type 4DE1	Num. of obs.	Best fit model
J13439+2538	13 43 56.7	25 38 47.7	0.087	A1	1	absorbed pl with bb
J13530+6918	13 53 03.4	69 18 30.6	0.031	B1	1	absorbed pl with bb
J13532+6345	13 53 15.9	63 45 46.0	0.088	B1	3	absorbed pl with bb
J13545+1805	13 54 35.7	18 05 18.1	0.1508	B1	2	absorbed pl with bb
J13590-4152	13 59 00.2	-41 52 52.4	0.3145	B1	1	absorbed pl with bb
J14052+2555	14 05 16.2	25 55 33.7	0.1633	A2	4	absorbed pl with bb
J14063+2223	14 06 21.9	22 23 46.7	0.0973	A2	2	-
J14070+2827	14 07 00.4	28 27 14.6	0.077	B1	1	double pl
J14138+4400	14 13 48.3	44 00 14.0	0.089	A1	1	double pl
J14179+2508*	14 17 59.6	25 08 12.7	0.0168	B1	18*	-
J14190-1310	14 19 03.8	-13 10 44.5	0.129	B1	1	absorbed pl with bb
J14275+2632	14 27 35.6	26 32 14.6	0.366	B1+	2	absorbed pl with bb
J14291+0117	14 29 06.6	1 17 06.2	0.086	B1	1	absorbed pl with bb
J14297+4747	14 29 43.1	47 47 26.4	0.221	A1	1	absorbed pl with bb
J14363+5847	14 36 22.1	58 47 39.4	0.033	B1	1	double pl
J14382-0658	14 38 16.2	-6 58 20.9	0.129	A1	2	absorbed pl with bb
J14421+3526	14 42 07.5	35 26 23.0	0.077	A2	5	absorbed pl with bb
J14511+2709	14 51 08.8	27 09 26.6	0.065	A2	2	absorbed pl with bb
J15040+1026	15 04 01.2	10 26 15.8	0.036	B1	5	absorbed pl with bb
J15313+0727	15 31 18.1	7 27 27.9	0.033	B2	1	absorbed pl with bb
J15366+5433	15 36 38.4	54 33 33.7	0.038	A1	6	-
J15477+2052	15 47 43.5	20 52 16.7	0.266	B1	1	absorbed pl with bb
J15591+3501	15 59 09.6	35 01 47.5	0.0313	A3	4	absorbed pl with bb
J16139+6543	16 13 57.4	65 43 10.2	0.129	B1+	2	absorbed pl
J16201+1724	16 20 21.8	17 36 23.9	0.5556	B1+	1	absorbed pl with bb
J16279+5522	16 27 56.1	55 22 31.6	0.132	B1	2	absorbed pl with bb
J16429+3948	16 42 58.8	39 48 36.9	0.594	B1	1	absorbed pl with bb
J17233+3417	17 23 20.7	34 17 58.3	0.206	A1	2	absorbed pl
J18219+6420	18 21 57.4	64 20 37.7	0.297	B1	5	absorbed pl with bb
J18350+3241	18 35 03.4	32 41 47.3	0.059	B1+	4	absorbed pl with bb
J18421+7946*	18 42 08.9	79 46 17.3	0.057	B1+	2*	-
J18449-6221	18 44 54.0	-62 21 53.4	0.014	A1	1	double pl
J20441-1043*	20 44 09.8	-10 43 24.3	0.035	A1	16*	-
J20463-0248	20 46 20.9	-2 48 44.9	0.027	A2	1	absorbed pl with bb
J21148+0607	21 14 52.6	6 07 41.8	0.4608	A2	6	double pl
J21324+1008	21 32 27.8	10 08 18.8	0.063	A1	2	absorbed pl with bb
J21377-1432	21 37 45.2	-14 32 55.8	0.2	B1+	1	absorbed pl with bb
J22032+3145	22 03 15.0	31 45 38.4	0.2952	A2	1	absorbed pl with bb
J22118+1841	22 11 53.9	18 41 49.9	0.07	B1	2	absorbed pl with bb
J22172+1414	22 17 12.3	14 14 20.9	0.067	B1	1	double pl
J22188-0335	22 18 52.0	-3 35 36.6	0.901	A1	1	absorbed pl with bb
J22426+2943	22 42 39.5	29 43 32.0	0.0245	A2	12	-
J22539+1608	22 53 57.8	16 08 53.6	0.8586	B1	4	absorbed pl with bb
J22540-1734	22 54 05.9	-17 34 55.8	0.0638	B1	9	-
J22541+1136	22 54 10.4	11 36 38.8	0.3256	B1	1	double pl
J22566+0525	22 56 36.4	5 25 16.9	0.065	A1	2	absorbed pl
J23032+0852	23 03 15.6	8 52 26.2	0.017	A1	8	-
J23070+0432	23 07 02.9	4 32 56.9	0.042	B1+	1	absorbed pl with bb
J23112+1008	23 11 17.7	10 08 15.8	0.432	B1+	1	absorbed pl with bb
SDSSJ010900.37+151217.5	1 09 00.5	15 12 18.1	0.3815	B1+	1	absorbed pl with bb

Name	RA	DEC	z	Spectral Type 4DE1	Num. of obs.	Best fit model
SDSSJ011703.58+000027.4	1 17 03.6	0 00 27.2	0.0456	A2	3	absorbed pl
SDSSJ013418.19+001536.8	1 34 18.2	0 15 36.7	0.4018	B1	2	absorbed pl
SDSSJ014017.07-005003.0	1 40 17.1	-0 50 02.9	0.3342	B1	1	absorbed pl with bb
SDSSJ014942.51+001501.7	1 49 42.6	0 15 00.9	0.5527	A2	3	absorbed pl
SDSSJ015530.03-085704.1	1 55 30.0	-8 57 04.1	0.1644	B1	1	absorbed pl
SDSSJ015950.25+002340.8	1 59 50.3	0 23 40.9	0.1631	A2	1	absorbed pl with bb
SDSSJ020615.99-001729.2	2 06 16.0	-0 17 28.5	0.0424	B1	3	absorbed pl with bb
SDSSJ024651.92-005931.0	2 46 51.9	-0 59 31.0	0.4687	A2	1	absorbed pl with bb
SDSSJ030000.01-080356.9	3 00 00.0	-8 03 57.0	0.5633	A3	1	double pl
SDSSJ074110.71+311200.2	7 41 10.7	31 12 00.2	0.632	B1	1	absorbed pl with bb
SDSSJ075101.42+291419.2	7 51 01.5	29 14 18.2	0.1209	A2	1	absorbed pl with bb
SDSSJ075525.29+391109.9	7 55 25.3	39 11 09.9	0.0337	A2	2	absorbed pl with bb
SDSSJ080101.41+184840.8	8 01 01.4	18 48 40.7	0.1398	A2	1	absorbed pl with bb
SDSSJ080908.13+461925.6	8 09 08.1	46 19 25.2	0.6587	A3	1	double pl
SDSSJ081456.09+532533.6	8 14 56.1	53 25 33.9	0.1197	A3	1	absorbed pl with bb
SDSSJ083535.81+245940.2	8 35 35.8	24 59 40.5	0.3297	A2	1	absorbed pl
SDSSJ083658.91+442602.3	8 36 58.9	44 26 02.7	0.2546	A1	1	absorbed pl with bb
SDSSJ090436.94+553602.6	9 04 37.0	55 36 02.8	0.0371	B1	1	absorbed pl with bb
SDSSJ092512.85+521710.5	9 25 12.9	52 17 10.3	0.0353	A1	5	-
SDSSJ092943.42+004127.3	9 29 43.4	0 41 27.4	0.5872	A2	1	absorbed pl with bb
SDSSJ093255.46+284036.8	9 32 55.5	28 40 38.1	0.5471	B1	1	-
SDSSJ093531.61+354101.0	9 35 31.6	35 41 01.9	0.496	A4	1	absorbed pl with bb
SDSSJ094033.75+462315.0	9 40 33.7	46 23 15.1	0.6972	A2	1	absorbed pl with bb
SDSSJ095048.39+392650.5	9 50 48.4	39 26 50.6	0.2059	B1	3	absorbed pl with bb
SDSSJ095931.67+504449.1	9 59 31.7	50 44 49.5	0.1434	A2	1	absorbed pl with bb
SDSSJ095955.85+130237.8	9 59 55.9	13 02 37.7	0.0354	A2	1	absorbed pl with bb
SDSSJ100420.13+051300.4	10 04 20.1	5 13 00.3	0.1611	A1	1	-
SDSSJ100726.10+124856.2	10 07 26.1	12 48 56.2	0.2406	B1	2	double pl
SDSSJ100854.93+373930.0	10 08 54.9	37 39 29.9	0.0536	A1	1	absorbed pl with bb
SDSSJ102531.28+514034.9	10 25 31.3	51 40 34.8	0.0449	A2	1	absorbed pl with bb
SDSSJ103059.10+310255.8	10 30 59.1	31 02 55.8	0.1782	B1	1	absorbed pl with bb
SDSSJ103312.51+501849.6	10 33 12.5	50 18 49.0	0.6612	B1	1	absorbed pl with bb
SDSSJ105143.90+335926.7	10 51 43.9	33 59 26.7	0.167	A1	1	absorbed pl with bb
SDSSJ110101.78+110248.9	11 01 01.8	11 02 48.1	0.0356	B1	1	absorbed pl with bb
SDSSJ111706.40+441333.3*	11 17 06.4	44 13 33.3	0.1439	B1	11*	-
SDSSJ111830.29+402554.0	11 18 30.3	40 25 54.0	0.1543	A2	1	absorbed pl with bb
SDSSJ111857.69+580323.7	11 18 57.7	58 03 23.6	0.0279	A1	2	absorbed pl with bb
SDSSJ112108.58+535121.1	11 21 08.8	53 51 21.6	0.103	A1	1	absorbed pl
SDSSJ112756.77+115427.1	11 27 56.8	11 54 27.2	0.5071	A2	1	absorbed pl with bb
SDSSJ114429.87+365308.6	11 44 29.7	36 53 08.9	0.0381	B1+	2	absorbed pl with bb
SDSSJ120114.36-034041.1	12 01 14.4	-3 40 41.1	0.0196	A1	4	absorbed pl with bb
SDSSJ120549.87+351046.0	12 05 49.9	35 10 45.8	0.0535	A1	2	absorbed pl with bb
SDSSJ120556.01+495956.2	12 05 56.0	49 59 56.3	0.0631	B1	1	-
SDSSJ121044.28+382010.3	12 10 44.3	38 20 10.9	0.0228	B1	1	double pl
SDSSJ121640.56+071224.3	12 16 40.6	7 12 24.3	0.5876	B1	1	absorbed pl
SDSSJ122011.88+020342.2	12 20 11.9	2 03 41.8	0.2404	B1	1	absorbed pl with bb
SDSSJ122106.87+454852.1	12 21 06.8	45 48 52.1	0.5252	B1	1	absorbed pl with bb
SDSSJ123054.12+110011.2	12 30 54.1	11 00 11.3	0.2362	B1	3	absorbed pl with bb
SDSSJ123413.34+475351.3	12 34 13.3	47 53 51.2	0.3723	B2	1	absorbed pl with bb
SDSSJ124210.61+331702.6	12 42 10.6	33 17 02.6	0.0435	A2	3	-

Name	RA	DEC	z	Spectral Type 4DE1	Num. of obs.	Best fit model
SDSSJ124635.25+022208.8	12 46 35.2	2 22 08.8	0.0482	A3	6	absorbed pl with bb
SDSSJ130028.53+283010.2	13 00 28.5	28 30 09.9	0.6471	B1+	2	absorbed pl with bb
SDSSJ130112.93+590206.7	13 01 12.9	59 02 06.7	0.4778	A3	1	absorbed pl with bb
SDSSJ134113.93-005315.0	13 41 13.9	-0 53 15.0	0.2368	A1	2	absorbed pl with bb
SDSSJ134749.86+582109.4	13 47 49.9	58 21 09.4	0.646	B1	1	absorbed pl with bb
SDSSJ134952.83+020445.1	13 49 52.8	2 04 45.1	0.0327	A1	1	double pl
SDSSJ135516.55+561244.7	13 55 16.5	56 12 45.2	0.1219	A2	2	absorbed pl with bb
SDSSJ135553.53+383428.7	13 55 53.5	38 34 28.3	0.0501	B1	1	absorbed pl with bb
SDSSJ141700.82+445606.4	14 17 00.8	44 56 06.4	0.1136	A3	1	absorbed pl with bb
SDSSJ142455.54+421407.6	14 24 55.5	42 14 07.7	0.3166	A2	2	absorbed pl with bb
SDSSJ143452.45+483942.8	14 34 52.5	48 39 42.3	0.0362	B1	1	absorbed pl with bb
SDSSJ144302.60+404525.1	14 43 02.6	40 45 25.0	0.2463	A3	1	absorbed pl with bb
SDSSJ144645.94+403505.7	14 46 46.0	40 35 05.8	0.267	A3	1	absorbed pl with bb
SDSSJ150556.55+034226.3	15 05 56.6	3 42 26.7	0.0361	B1	1	absorbed pl with bb
SDSSJ151443.07+365050.4	15 14 43.1	36 50 50.5	0.3707	B1	1	absorbed pl with bb
SDSSJ153552.40+575409.5	15 35 52.4	57 54 09.5	0.0296	B1	4	-
SDSSJ154530.24+484609.1	15 45 30.2	48 46 08.9	0.4014	A2	4	absorbed pl
SDSSJ161413.21+260416.2	16 14 13.2	26 04 16.3	0.131	A1	1	absorbed pl with bb
SDSSJ215014.77-065314.5	21 50 14.7	-6 53 13.5	0.5906	A1	1	absorbed pl
SDSSJ223607.68+134355.3	22 36 07.7	13 43 55.4	0.3265	A2	1	absorbed pl with bb
SDSSJ230443.47-084108.6	23 04 43.5	-8 41 08.6	0.0469	B1+	1	absorbed pl with bb
SDSSJ232259.99-005359.2	23 23 00.0	-0 53 59.2	0.1506	A3	1	absorbed pl with bb

Table 7: The 186 sources from Zamfir et al. (2010), Sulentic et al. (2007), Marziani et al. (2003) used in this work. Objects marked with * correspond to the variable sources mentioned in Table 5. "Best fit model" column presents the preferred model for each source: absorbed power-law, absorbed power-law with black-body or double power-law. The hyphen (-) is used for sources that need a more complex model.